



Magnesite formation in playa environments near Atlin, British Columbia, Canada

Ian M. Power^{a,*}, Anna L. Harrison^b, Gregory M. Dipple^a, Siobhan A. Wilson^c
Shaun L.L. Barker^d, Stewart J. Fallon^e

^a Department of Earth, Ocean and Atmospheric Sciences, The University of British Columbia, Vancouver, British Columbia V6T 1Z4, Canada

^b Department of Geological Sciences and Geological Engineering and the School of Environmental Studies, Queen's University, Kingston, Ontario K7L 3N6, Canada

^c Department of Earth and Atmospheric Sciences, University of Alberta, Edmonton, Alberta T6G 2E3, Canada

^d School of Natural Sciences (Earth Sciences), University of Tasmania, Hobart, Tasmania 7001, Australia

^e Research School of Earth Sciences, The Australian National University, Canberra, ACT 0200, Australia

Received 20 December 2017; accepted in revised form 7 April 2019; Available online 13 April 2019

Abstract

The hydromagnesite–magnesite playas near Atlin, British Columbia, Canada are unique Mg-carbonate depositional environments that have formed at Earth's surface since the end of the last deglaciation. This study elucidates the mechanisms, pathways, and rates of magnesite (MgCO_3) formation in these near-surface environments, which are challenging to study in short-duration laboratory experiments because magnesite precipitation is extremely slow at low temperature. The Atlin playas, having formed over millennia, contain abundant magnesite as well as a suite of other Mg- and Ca-carbonate minerals. Mineralogical and textural evidence demonstrate that hydromagnesite [$\text{Mg}_5(\text{CO}_3)_4(\text{OH})_2 \cdot 4\text{H}_2\text{O}$] forms at least in part through transformation of more hydrated phases, e.g., lansfordite ($\text{MgCO}_3 \cdot 5\text{H}_2\text{O}$). Deposition of these hydrated Mg-carbonate minerals is limited by the evaporative flux, and thus, is effectively transport-controlled at the scale of the playas. Magnesite is a spatially distinct phase from hydromagnesite and its crystal morphology varies with depth indicating variable crystal growth mechanisms and precipitation rates. Particle size distributions and mineral abundance data indicate that magnesite formation is nucleation-limited. Furthermore, mineralogical data as well as stable and radiogenic isotope data support magnesite formation starting after the majority of hydromagnesite had been deposited likely resulting from long induction times and slow precipitation rates. Hydrated Mg-carbonate minerals precipitate relatively rapidly and control pore water chemistry while magnesite remains highly supersaturated, and thus, is reaction-controlled. This difference in controlling regime allows for magnesite abundance to increase over time without the loss of hydromagnesite such as through its transformation, which the data also does not support. We estimate rates of magnesite formation (nucleation + crystal growth) in the range of 10^{-17} to 10^{-16} mol/cm²/s over approximately 8000 years. This study helps to elucidate the geochemical conditions needed to form Mg-carbonate minerals in ancient and modern sedimentary environments and provides insights into facilitating long-term storage of anthropogenic CO₂ within Mg-carbonate minerals.

© 2019 Elsevier Ltd. All rights reserved.

Keywords: magnesite; hydromagnesite; playas; mineral formation rates; CO₂ sequestration

* Corresponding author at: Trent School of the Environment, Trent University, Peterborough, Ontario K9L 0G2, Canada.

E-mail addresses: ianpower@trentu.ca (I.M. Power), anna.harrison@queensu.ca (A.L. Harrison), gdipple@eoas.ubc.ca (G.M. Dipple), sawilson@ualberta.ca (S.A. Wilson), shaun.barker@utas.edu.au (S.L.L. Barker), stewart.fallon@anu.edu.au (S.J. Fallon).

1. INTRODUCTION

Magnesite (MgCO_3) formation is kinetically controlled at low temperature (i.e., $<60^\circ\text{C}$), which has greatly hindered understanding of its formation pathways and the determination of its formation rates at Earth's surface conditions (Christ and Hostetler, 1970; Königsberger et al., 1999; Hänchen et al., 2008). The strong hydration of Mg^{2+} ions in solution causes this kinetic inhibition (Königsberger et al., 1999; Hänchen et al., 2008). Consequently, numerous metastable hydrated Mg-carbonate phases are more commonly formed at low temperature. Recent studies have demonstrated that carboxylated compounds can dehydrate Mg^{2+} ions and promote magnesite formation (e.g., Power et al., 2017b; Miller et al., 2018). Further complicating the understanding of magnesite formation are the various phase transformations that may occur between Mg-carbonate minerals. These transformations depend on a variety of environmental and geochemical factors including temperature, water availability, CO_2 partial pressure, and Mg concentration (Königsberger et al., 1999; Hänchen et al., 2008; Hopkinson et al., 2012; Di Lorenzo et al., 2014; Montes-Hernandez and Renard, 2016). It remains unclear as to whether magnesite predominantly forms via decomposition of a hydrated precursor phase, e.g., hydromagnesite [$\text{Mg}_5(\text{CO}_3)_4(\text{OH})_2 \cdot 4\text{H}_2\text{O}$] or is a primary precipitate in Earth's surface environments. The formation pathway has implications for the rate of magnesite formation.

The hydromagnesite–magnesite playas near Atlin, British Columbia, Canada host a complex assemblage of Mg-carbonate minerals that have formed at Earth's surface over millennia (Power et al., 2009; Power et al., 2014). These environments are ideal for studying the Mg-carbonate system, and particularly the formation of magnesite and hydromagnesite. This study advances the understanding and interpretation of modern (i.e., Holocene epoch) sedimentary magnesite-forming environments (e.g., Renaut and Long, 1989; Renaut, 1993; Wright and Wacey, 2005; Mees and Keppens, 2013) and ancient magnesite deposits (e.g., Garber et al., 1990; Spötl and Burns, 1994; Melezhik et al., 2001; Alçiçek, 2009).

Magnesium carbonate formation and diagenesis are of particular interest because of their relevance to *ex situ* carbon mineralization and subsurface geologic carbon storage as strategies for reducing net greenhouse gas emissions (Lackner et al., 1995; Power et al., 2009; Power et al., 2013b). The Atlin playas are a natural analogue for storage of CO_2 in Mg-carbonate minerals, the end-product of several engineered carbon mineralization strategies for CO_2 storage, and provide insights into the geochemical conditions that control Mg-carbonate formation and the mineral phase transformations that may occur through diagenesis. The study of the Atlin playas is particularly relevant to the numerous proposed strategies for storing CO_2 in Mg-carbonate minerals at low temperature and pressure (e.g., Ferrini et al., 2009; Wilson et al., 2009a; Power et al., 2010; Zhao et al., 2010; Power et al., 2011; Pronost et al., 2011; Bea et al., 2012; Beinlich and Austrheim, 2012; Harrison et al., 2013a; Power et al., 2013a; Wilson et al.,

2014; Zarandi et al., 2017). The persistence of the Atlin playas since from the last deglaciation (~ 11 ka) to present day suggests that Mg-carbonate minerals provide the level of stability required of anthropogenic CO_2 sinks to prevent CO_2 leakage. Magnesite is the most stable Mg-carbonate (Königsberger et al., 1999), making it ideal for the long-term storage of CO_2 compared to the metastable hydrated minerals.

The goal of this study is to elucidate the mechanisms and rates of hydromagnesite and magnesite formation at low temperature. Specifically, we aim to: (1) characterize magnesite and hydromagnesite abundance, distribution, crystal morphology, and isotopic composition; (2) elucidate the modes of formation of magnesite and hydromagnesite (i.e., transformation versus direct precipitation); (3) compare the relative rates of magnesite and hydromagnesite formation; and (4) quantify magnesite formation rates. The findings from this study have implications for interpreting the geochemical conditions of magnesite-forming environments in the present and geologic past, as well as the development of low-temperature carbon sequestration strategies for long-term storage of CO_2 within Mg-carbonate minerals.

2. GEOLOGIC SETTING AND PLAYA DEPOSITIONAL MODEL

Hydromagnesite–magnesite playas are found near the town of Atlin in northwestern British Columbia, Canada (Fig. 1a; $59^\circ 34'\text{N}$, $133^\circ 42'\text{W}$). The Atlin area has been the site of numerous geologic investigations relating to the regional geology including the origin of ophiolitic ultramafics (Aitken, 1959; Bloodgood et al., 1989; Ash and Arksey, 1990a; Ash et al., 1991; Mihalynuk et al., 1992; Ash, 1994), listwanite-lode gold deposits (Ash and Arksey, 1990b; Ash, 2001), Upper Paleozoic rocks of the Atlin Terrane (Monger, 1975; Monger, 1977a,b; Monger et al., 1978), occurrence of lansfordite ($\text{Mg}_3\text{CO}_3 \cdot 5\text{H}_2\text{O}$) (Poitevin, 1924), and the first documentation of the hydromagnesite–magnesite playas (Young, 1916). More recently, Hansen et al. (2005) described the geologic setting of listwanite (carbonated serpentinite) and its implications for high-temperature mineral carbonation as well as lode-gold mineralization. We have previously proposed biogeochemical (Power et al., 2009) and depositional (Power et al., 2014) models for the playas; the latter is summarized here to place the formation of hydromagnesite and magnesite into the context of playa genesis.

The ultramafic complex near Atlin consists of a tectonically emplaced upper mantle section of oceanic lithosphere, which is mainly composed of serpentinite and listwanite that predominantly transformed from harzburgite and minor dunite (Ash and Arksey, 1990a; Hansen et al., 2005). The weathering of ultramafic bedrock produces Mg– HCO_3 groundwater that discharges into topographic lows where the playas lie (Power et al., 2009; Power et al., 2014). There are two groups of playas (total area ≈ 11 ha) that are immediately east of Atlin. The northern playa is the largest and has several small satellite playas nearby. The southern group consists of two playas, referred

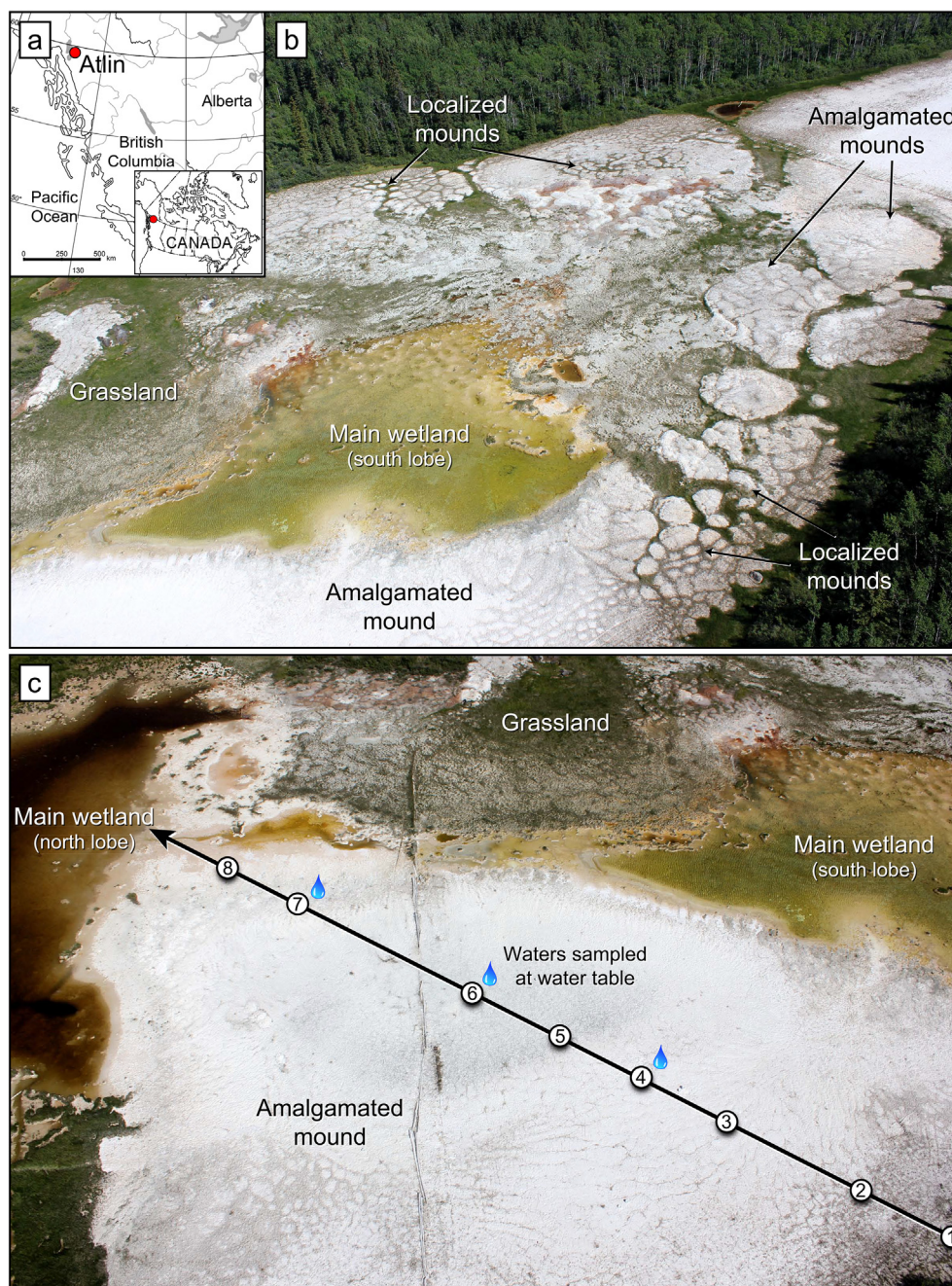


Fig. 1. (a) Location of Atlin, British Columbia, Canada. (b) Aerial photograph of the southeastern playa showing the four surface environments: wetland, grassland, localized mounds and amalgamated mounds. (c) Photograph of the amalgamated mound adjacent to the main wetland showing the locations of the eight sediment profiles (see Fig. 2). Water samples were collected from the water table at profiles 4, 6 and 7.

to as the southwestern and southeastern playas that are separated by a ridge (Fig. 1b and c shows the southeastern playa). In addition to these playas, there are numerous alkaline water bodies in the Atlin region including Como Lake and Moose Lake (Power et al., 2009). The playas host a wide range of magnesium and calcium carbonate minerals that form in a variety of environments (Table 1).

The southeastern playa has four surface environments (wetlands, grasslands, localized hydromagnesite–magnesite

mounds, and amalgamated hydromagnesite–magnesite mounds) representing various stages of playa genesis (Fig. 1b). Mineralogical analysis of sediments revealed three consecutive sedimentary units: Mg-carbonate sediments, Ca-Mg-carbonate sediments, and glaciolacustrine mud, from the surface to ~4 m depth (Power et al., 2014). Fig. 2 is reproduced and modified from Power et al. (2014) with additional annotations and inclusion of profile 8. Glaciolacustrine, siliceous mud was deposited first

Table 1
Relevant carbonate minerals in playas.

Mineral	Formula	Location in the playas
Lansfordite	$Mg_3CO_3 \cdot 5H_2O$	Hardpan at water table within mounds
Nesquehonite	$Mg_3CO_3 \cdot 3H_2O$	Surface crusts near waters and films on water surface; trace amounts in hardpan
Dypingite	$Mg_5(CO_3)_4(OH)_2 \cdot 5H_2O$	Benthic mats and surface sediments along wetland periphery
Hydromagnesite	$Mg_5(CO_3)_4(OH)_2 \cdot 4H_2O$	Grassland sediments (above water table), mounds (Mg-carbonate unit)
Magnesite	$MgCO_3$	Mounds (Mg-carbonate and Ca-Mg-carbonate units)
Dolomite (or high Mg-calcite)	$CaMg(CO_3)_2$	Ca-Mg-carbonate sediments that underlie Mg-carbonate sediments in mounds
Huntite	$CaMg_3(CO_3)_4$	Possibly present in Ca-Mg-carbonate sediments
Ankerite	$Ca(Fe^{2+}, Mg, Mn)(CO_3)_2$	Sediments below the water table in the grassland areas
Aragonite	$CaCO_3$	Anoxic sediments in wetland below benthic mats; consolidated aragonite along wetland periphery; pisolites; Ca-Mg-carbonate unit

in glacial lakes that occupied topographic lows carved out during the last glaciation. Over time, carbonate deposition overtook siliciclastic deposition as the supply of glacial meltwater ceased and was replaced by alkaline Mg–HCO₃ groundwater.

Modern groundwater (pH ≈ 8.1) near the playas is supersaturated with respect to anhydrous carbonate minerals: aragonite, calcite, dolomite, huntite, and magnesite. Upon discharging into alkaline ponds, carbonate precipitation is driven by chemical and physical processes (e.g., CO₂ degassing and evaporation) as well as biological processes (e.g., alkalization by photosynthetic microbes; Power et al., 2007), which fills these water bodies with carbonate sediment over time. Small (metre-scale) and larger (~0.2 ha) water bodies still occupy the modern southeastern playa, which has no surface inflows or outflows, thereby creating an endorheic basin that concentrates waters through evaporation. The main wetland (pH ≈ 8.6) is supersaturated with respect to the aforementioned carbonate minerals as well as hydromagnesite and lansfordite and is near saturation with respect to nesquehonite. However, anoxic sediments below microbial mats in the pond are undersaturated with respect to these hydrated Mg-carbonate minerals due to a lower pH value of ~7. Subaqueous carbonate deposition progressively fills these ponds with mainly aragonite, and through diagenesis a Ca-Mg-carbonate unit comprised of aragonite, ankerite, dolomite (or high Mg-calcite), and magnesite forms overlying the glaciolacustrine deposit. Buried grass near the top of this Ca-Mg-carbonate unit indicates that there was a transition from subaqueous to subaerial sediment deposition. Mg–HCO₃ waters are drawn to the surface by capillary action and evaporate in the unsaturated zone leading to subaerial precipitation of hydrated Mg-carbonate minerals and development of nearly pure hydromagnesite mounds. Continued precipitation grows these mounds upward and laterally, thereby amalgamating metre-scale mounds into larger mounds that are 10 s of metres in diameter in the present day (Fig. 1b and c).

With regards to timing, all carbonate sediments overlay glaciolacustrine sediments that were deposited during the last deglaciation in which the Cordilleran ice sheet reached a maximum size at approximately 16.5 ka and had disappeared by ~11 ka (Menounos et al., 2009 and references

therein). Radiocarbon dating of buried vegetation at the top of the Ca-Mg-carbonate unit indicates that deposition of the overlying Mg-carbonate unit began upwards of ~8000 cal yr BP and its deposition rate has been ~0.4 mm/yr (Power et al., 2014). The depositional model constrains magnesite formation to the Holocene and an Earth surface temperature.

3. METHODS

3.1. Field methods

3.1.1. Water sampling

Waters in the Atlin area were sampled for ¹⁴C analyses. These included spring water collected at the base of Monarch Mountain (~3.5 km to the southeast of the playas), groundwater from a private well, and the playa water table. The well (~35 m deep) was located approximately 50 m from the southeastern playa and was flushed several times to obtain representative groundwater. A 60 mL syringe and Tygon™ tubing were used to collect samples from the water table beneath the amalgamated mound during sediment sampling using an auger at the locations of profiles 4, 6, and 7 (Fig. 1c). In addition, samples from the water table were collected from a 20 cm deep hole dug near the wetland periphery, and ~1-metre-deep pit approximately 30 m from the south lobe of the main wetland. The pond water from the main wetland in the southeastern playa was also sampled. All water samples were filtered (0.22 μm) into TraceClean™ 40 mL amber borosilicate vials with a fluoropolymer resin/silicone septum and no headspace. Additional water samples for analyses of cations, anions and dissolved inorganic carbon (DIC) were collected from the water table at profiles 6 and 7. These samples were filtered (0.22 μm) into 2 mL borosilicate glass vials with cation samples being acidified to 2% v/v ultrapure nitric acid. A Thermo Scientific® Orion 4-Star portable pH/ISE meter was used to measure pH in the field and samples were stored at 4 °C before analysis.

3.1.2. Sediment sampling

Sediment sampling was mainly conducted in the southeastern playa (Fig. 1b). These sediments were predominantly hydromagnesite and magnesite (see Power et al.,

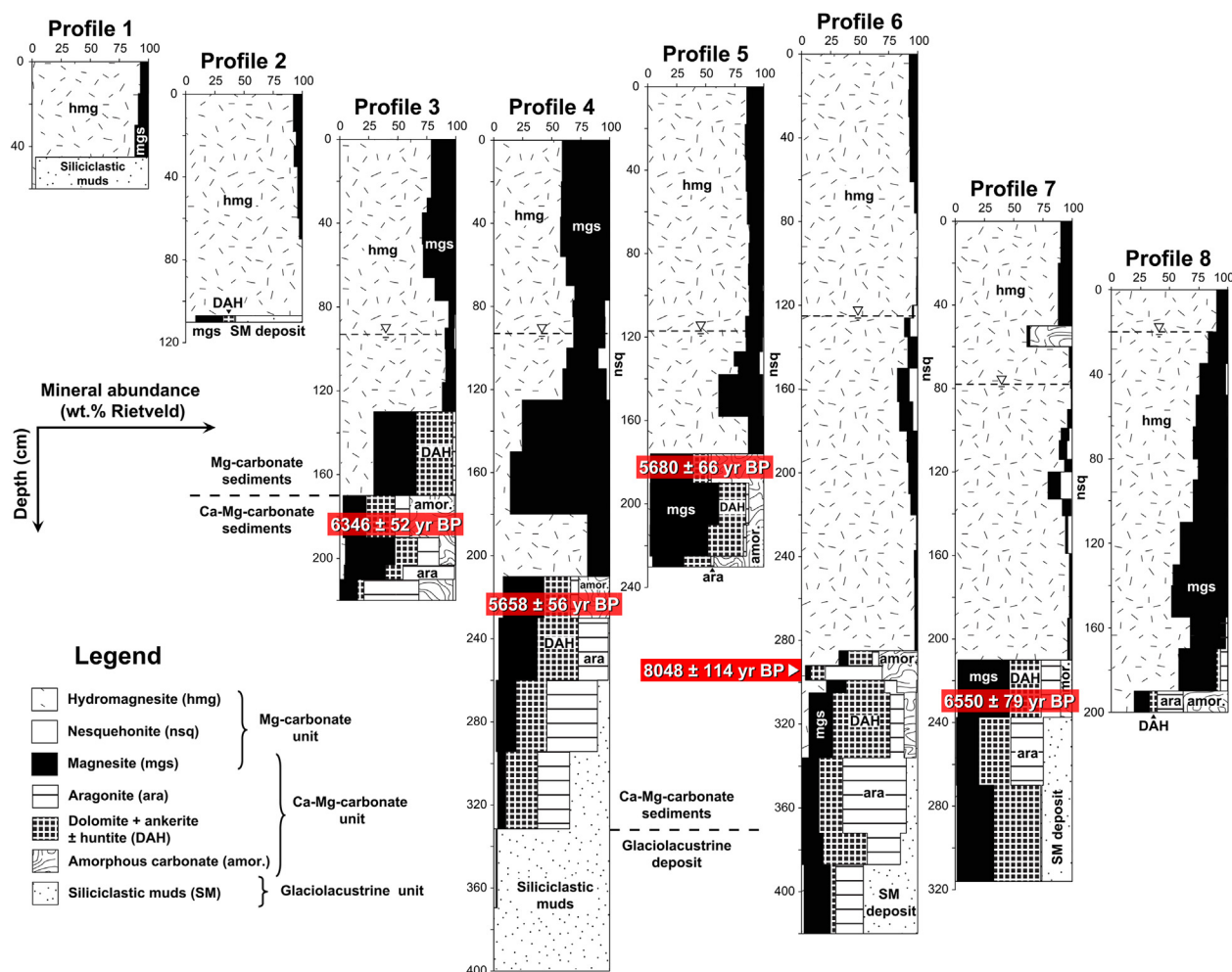


Fig. 2. Mineral abundance profiles of the playa along the sampling transect (Fig. 1c). Mineral abundances (wt.%) versus depth (cm). The minerals plotted include hydromagnesite (hmg), magnesite (mgs), nesquehonite (nsq), aragonite (ara), dolomite, ankerite and huntite (grouped as DAH), and silicate minerals grouped as siliciclastic muds. Data of sediment samples near the water table do not accurately represent the mineralogical compositions of these sediments. Samples were stored at room temperature for approximately 1 yr prior to analysis, which resulted in lansfordite dehydrating to nesquehonite and hydromagnesite. Subsequent analyses of fresh sediments near the water table that form a hardpan showed they contained 36 wt.% lansfordite and trace nesquehonite (~ 3 wt.%). The calibrated ages based on radiocarbon analyses of organics are labelled on profiles 3 through 7. The sediment profiles are positioned vertically based on their relative elevations (modified from Power et al., 2014).

2014 for details). Previous sampling along a 75 m north-trending transect consisted of samples from profiles 1 (playa margin) through 7 (near wetland; Power et al., 2014) with profile 8 being added to this study (Fig. 1c). Samples at depth (up to 4 m) were collected using an auger. At the time of sampling, a thermometer was inserted into the sediments from profile 4 to measure temperature.

Selective sampling was conducted in the main wetland and surrounding area for additional ^{14}C analyses. Benthic mats and underlying anoxic black sediments were collected from the main wetland pond in addition to evaporative surface crusts near the wetland periphery. Sediments from the surface and below the water table at 40 cm depth in the grassland environment were sampled as well as a pisolite from consolidated aragonite rubble between localized mounds of hydromagnesite. Consolidated Mg-carbonate

sediments that form a hardpan near the water table of the amalgamated mound at the location of profile 7 were sampled. Samples were collected in either plastic bags or 50 mL centrifuge tubes. Fieldwork and sampling for this study were conducted in July of 2011 and 2012.

3.2. Analytical methods

3.2.1. Water analyses

At The University of British Columbia, cations were analyzed using inductively coupled plasma optical emission spectrometry (ICP-OES) employing a Varian 725-ES Optical Emission Spectrometer. Reproducibility was better than $\pm 5\%$ relative error based on repeated analysis of standards and duplicate samples. Anions were analyzed using ion chromatography by ALS Environmental in Burnaby, Bri-

tish Columbia with reproducibility being better than $\pm 5\%$ relative error based on repeated analysis of duplicate samples. DIC concentrations were determined using a Lachat IL550 TOC-TN analyzer (Hach Company, Loveland, CO, USA). Aliquots (100 μL) of sample were added to a 10% H_3PO_4 by volume solution to release $\text{CO}_2(\text{g})$, which was measured with an infrared detector. The detection limit for this instrument is 0.5 mg/L. These water chemical data from the water table at profiles 6 and 7 supplemented previously published data (Power et al., 2014; Table 2).

Mineral saturation indices were calculated using PHREEQC V3 (Parkhurst and Appelo, 2013) and the LLNL database, which was modified to include the carbonic acid dissociation constants of Patterson et al. (1982, 1984), the thermodynamic constant for Mg^{2+} hydrolysis (Palmer and Wesolowski, 1997), and the magnesite and hydromagnesite solubility products of Bénézeth et al. (2011) and Gautier et al. (2014), respectively. The aqueous MgHCO_3^+ and MgCO_3^0 complexes were added after Stefánsson et al. (2014). Activity coefficients were calculated using the PHREEQC LLNL database.

3.2.2. X-ray diffraction methods

Select sediment samples that were treated with dilute acid were analyzed by X-ray diffraction (XRD) to confirm the removal of hydromagnesite prior to isotopic analysis. Finely ground aliquots were mounted as slurries onto glass plates with anhydrous ethanol and allowed to dry at room temperature. All XRD data were collected using a Bruker D8 Focus Bragg-Brentano diffractometer with a step size of 0.04° over a range of $3\text{--}80^\circ 2\theta$ at 0.8 s/step and a sample rotation of 50 rpm. A Fe monochromator foil, a 0.6 mm divergence slit, incident and diffracted beam Soller slits, and a Lynx Eye position sensitive detector were used to collect patterns. A long, fine-focus Co X-ray tube was operated at 35 kV and 40 mA using a take-off angle of 6° . Search-match software, DIFFRACplus EVA 14, and the International Centre for Diffraction Database PDF-4+ 2010 were used for phase identification (Bruker, 2008). Mineral abundances in profile 8 samples were determined using the same methods as for the other profile samples (refer to Power et al., 2014 and references therein). Rietveld refinements for profile 8 samples were completed using Topas Version 3 software (Bruker, 2004).

At The University of British Columbia, our Rietveld refinement analyses can accurately quantify carbonate abundance to a lower limit of ~ 0.5 wt.%, and the quantification of crystalline carbonate abundance (e.g., nesquehonite) of <10 wt.% is approximately 15% relative error (Wilson et al., 2006, 2009b). Additionally, the results of Wilson et al. (2006) indicate that an effective lower limit for quantification of amorphous content may be ~ 5 wt.%.

3.2.3. Microscopy

Petrographic thin sections of the hardpan, collected at profile 7, were imaged using a Nikon petrographic microscope equipped with a Canon EOS Rebel T2i camera. Scanning electron microscopy (SEM) of sediment samples was performed at the Centre for High-Throughput Phenogenomics at The University of British Columbia, Vancouver,

Canada. Samples were mounted onto aluminum stubs using 12 mm carbon adhesive tabs and coated with iridium (8 nm) using a Leica EM MED020 coating system. Imaging was performed using an FEI Helios NanoLab 650 emission SEM, with an operating voltage of 1.0 kV.

3.2.4. Sediment physical properties and water contents

The porosity of the near-surface Mg-carbonate unit was estimated by gravimetric measurements of known volumes ($n = 8$) of sediment that were weighed before and after drying at room temperature. This sediment density was compared to that of stoichiometric hydromagnesite to calculate the porosity. Sediments from profile 4 were dried first at room temperature and then at 105°C to determine sediment and crystallographic water contents, respectively. Any lansfordite, nesquehonite, or dypingite present in the samples was converted to hydromagnesite when the sediments were heated to 105°C until masses stabilized after approximately 4 days.

Surface areas of samples containing 100 wt.% hydromagnesite (profile 2, ~ 80 cm depth) and 96 wt.% magnesite (collected from the North playa at a depth of ~ 95 cm) were determined by multipoint Brunauer–Emmett–Teller (BET; Brunauer et al., 1938) with N_2 adsorption using a Quantachrome® Autosorb-1 surface area analyzer. Prior to the BET measurement, trace amounts of organics were removed from the magnesite sample by reacting it with 30% hydrogen peroxide solution for one day as per the methodology of Feller et al. (1992). Reproducibility was better than $0.1\text{ m}^2/\text{g}$ based on repeated analysis of duplicate samples. To estimate the particle size distribution of magnesite in sediments containing both magnesite and hydromagnesite, 10% HCl was used to dissolve the hydromagnesite until vigorous fizzing had ceased. The sediments were rinsed with deionized water to prevent further reaction. The absence of hydromagnesite was confirmed using XRD. Particle size analyses were then performed using a Malvern® Mastersizer 2000 Laser Diffraction Particle Size Analyzer. The standard deviations ranged from 0.006 to $0.34\ \mu\text{m}$ based on triplicate analyses. It was expected that smaller magnesite grains may have dissolved, and larger grains may have been reduced in size. All of these analyses were conducted at The University of British Columbia.

3.2.5. Stable isotope analyses

Stable carbon and oxygen isotopes were measured at The University of British Columbia. Hydromagnesite dissolves much more rapidly than magnesite, allowing for separate analysis of the stable carbon and oxygen isotopic compositions in mixtures containing both minerals (refer to methods in Wilson et al., 2014). Aliquots (10–100 mg) of sediment were placed in Labco Exetainer® vials and acidified using 85% phosphoric acid (H_3PO_4). For hydromagnesite analyses, samples were reacted at room temperature ($\sim 25^\circ\text{C}$) for 1 h immediately prior to analysis. For magnesite analyses, evolved CO_2 from the rapid reaction of hydromagnesite was allowed to escape for 30 min. Qualitative X-ray powder diffraction data were collected on a subset of samples to confirm the removal of hydromagnesite using similar methods as previously described. Sample

Table 2

Water chemistry of the southeastern playa near Atlin, British Columbia. Detection limits are given in parentheses and analytes not detected are listed as “n.d.” PHREEQC (Parkhurst and Appelo, 2013) was used to calculate saturation indices for lansfordite (lns), nesquehonite (nsq), hydromagnesite (hmg), and magnesite (mgs).

Sample location	pH	Alkalinity (mg HCO ₃ ⁻ /L)	Cation concentrations (mg/L)							Anion concentrations (mg/L)		
			Mg (0.1)	Ca (0.2)	Si (0.3)	Na (0.2)	K (1.0)	Fe (0.1)	Al (0.7)	SO ₄ (0.1)	Cl (0.1)	NO ₃ (0.1)
Groundwater well ^a	8.14	2610	474	7.3	11.5	16.1	6.8	n.d.	0.16	39.8	1.9	0.1
Mound waters												
Profile 4 location ^a	7.98	8480	1547	2.1	16.7	87.4	14.3	0.22	0.25	77.4	7.4	4.1
Profile 6 location	8.14	6698	1885	1.3	6.7	79.4	13.0	n.d.	n.d.	26.3	8.7	2.7
Profile 7 location	8.17	5995	1675	0.4	n.d.	109	16.5	n.d.	n.d.	36.9	18.4	5.4
Wetland (north lobe) ^a	8.61	4780	887	9.9	31.1	57.5	11.0	0.15	0.26	97	16.6	n.d.
Wetland (south lobe) ^a	8.56	4720	865	9.2	33.8	76.1	12.4	n.d.	0.26	80.5	6.4	n.d.
Sample location	Saturation indices											
	Lns			Nsq				Hmg			Mgs	
Groundwater well	-0.31			-1.49				-3.38			1.45	
Mound waters												
Profile 4 location	0.29			-0.67				-0.11			2.19	
Profile 6 location	0.43			-0.75				0.05			2.19	
Profile 7 location	0.42			-0.76				0.01			2.18	
Wetland (north lobe)	0.47			-0.48				1.72			2.38	
Wetland (south lobe)	0.42			-0.53				1.42			2.33	

^a Data from Power et al. (2014).

vials were then sealed, and the magnesite was reacted at 72 °C overnight to ensure complete reaction. The CO₂ generated from the acidification of all carbonate samples was passed through an ethanol–dry ice cold trap, and subsequently mixed with ~100 mL of laboratory air, before being drawn into a Los Gatos Research (LGR[®]) off-axis integrated cavity output laser spectrometer (detailed methods provided by [Barker et al., 2011](#)). The LGR instrument measures the absorption spectra of ¹²C¹⁶O¹⁶O, ¹³C¹⁶O¹⁶O, and ¹²C¹⁶O¹⁸O in the near-infrared wavelength spectrum. The stable carbon and oxygen isotope values are reported in the conventional δ notation in per mil (‰) relative to Vienna Pee Dee Belemnite (VPDB) and Vienna Standard Mean Ocean Water (VSMOW), respectively. An in-house calcite standard with a well-known δ¹³C_{VPDB} value of 1.8 ± 0.2‰ and δ¹⁸O_{VSMOW} value of 13.7 ± 0.3‰ was measured at least every five samples. The δ¹⁸O values of Mg-carbonate sediments were corrected for reaction with phosphoric acid using the fractionation factors from [Das Sharma et al. \(2002\)](#). The fractionation factor for magnesite was used as a proxy for the fractionation of hydrated Mg-carbonate minerals. These factors were $10^3 \ln \alpha_{\text{CO}_2\text{-mgs}} = 11.920\text{‰}$ at 25 °C (hydromagnesite) and 9.966‰ at 72 °C (magnesite). Stable carbon and oxygen isotope data for hydromagnesite and magnesite in the sediment mixtures were compared to isotope data previously reported for the same bulk sediment samples ([Power et al., 2014](#)). In this comparison, predicted δ¹³C and δ¹⁸O values of the bulk sediment mixtures were calculated based on the molar carbon and oxygen ratios and relative abundances of hydromagnesite and magnesite as determined by Rietveld refinement of XRD data. These calculated isotope values were in good agreement (<10% relative error) with the previously measured values for the bulk sediments ([Power et al., 2014](#)).

3.2.6. ¹⁴C analysis

Sediment samples that contained organics from sediment profiles 3, 4 and 5 were analyzed at the Radiocarbon Dating Centre at the Australian National University, Canberra. Organic matter in the sediments was isolated using an acid/base/acid wash treatment that alternated between 1M HCl and 1M NaOH in 30 min batches until wash solutions were clear. A final 1 h acid wash was performed. Samples were rinsed with Milli-Q[™] water until the supernatant was neutral and then dried overnight. A standard procedure for sample combustion and CO₂ purification was conducted and followed by graphitization using the method of [Santos et al. \(2004\)](#). ¹⁴C analyses were performed using a single-stage accelerator mass spectrometer ([Fallon et al., 2010](#); [Beavan et al., 2012](#)). Sample preparation backgrounds were subtracted based on measurements of samples of ¹⁴C-free CO₂. Standard deviations of calibrated ages ranged from 52 to 114 years before present. In addition, radiocarbon analysis of water samples by Accelerator Mass Spectrometry was performed at the NSF Accelerator Mass Spectrometry Laboratory, University of Arizona, Tucson, USA. Percent modern carbon data were reported with errors of ±0.1.

4. RESULTS

4.1. Mound pore waters

Mg–HCO₃ groundwater that discharges into the playas was undersaturated with respect to hydrated Mg-carbonate minerals, yet supersaturated with respect to magnesite ([Table 2](#); [Power et al., 2009](#); [Power et al., 2014](#)). In contrast, playa surface waters were also supersaturated with respect to hydromagnesite, lansfordite and nearly saturated with respect to nesquehonite (nesquehonite films occasionally form on water surfaces; [Power et al., 2009](#)). Waters collected from the water table of the amalgamated mound ([Fig. 1c](#)) were at equilibrium with hydromagnesite [avg. saturation index (SI) = 0.0] and supersaturated with respect to lansfordite (avg. SI = 0.4) and magnesite (avg. SI = 2.2; [Table 2](#)).

During the summer, the sediment temperature at the water table was approximately 6 °C with temperatures ranging from 14 °C at the surface to 3 °C at a depth of 180 cm in profile 4 ([Fig. 3](#)), the deepest measurement taken. Water contents of sediments in profile 4 ranged from 35% to 50% as a percentage of total sediment mass ([Fig. 3](#)). Furthermore, water saturation was relatively consistent throughout the unsaturated zone.

4.2. Mineralogical and textural data

The most striking features of the playas are the localized and amalgamated mounds of hydromagnesite and magnesite that give rise to a hummocky surface topography ([Fig. 1b](#)). Importantly, the few localized mounds that have been sampled were entirely composed of hydromagnesite ([Power et al., 2009](#)), whereas the amalgamated mounds were predominately hydromagnesite with variable amounts of magnesite ([Power et al., 2014](#)). The upper surface of the large amalgamated mound where most of the sampling was conducted was 1–2 m above the wetland water surface ([Fig. 1c](#)). At the location of the sampling transect, hydromagnesite abundance at the surface ranged from 59 to 92 wt.% with the remainder being magnesite (8–41 wt.%; see [Power et al., 2014](#)). The sampling transect intersected two magnesite-rich zones, one centered on profile 4 and another at profile 8 ([Fig. 1c](#); [Power et al., 2014](#)). High magnesite abundance at the surface of a profile correlated with relatively high magnesite abundance at depth ([Fig. 2](#)).

Profiles 3 through 8 extended below the water table (~1 m), which was located within the Mg-carbonate unit ([Fig. 2](#)). The sediments near the water table had a distinct mineralogical composition and formed a hardpan (20–30 cm thick). Data presented in [Fig. 2](#) does not accurately represent sediments near the water table as samples were stored at room temperature for >1 year before analysis, which resulted in lansfordite dehydrating to nesquehonite and hydromagnesite prior to analysis ([Power et al., 2014](#)). Analyses of fresh samples (n = 3) demonstrated that the hardpan contained an average of 36 wt.% lansfordite and trace amounts of nesquehonite (~3 wt.%; [Power et al., 2014](#)). Lansfordite formed mm-scale, prismatic crystals that

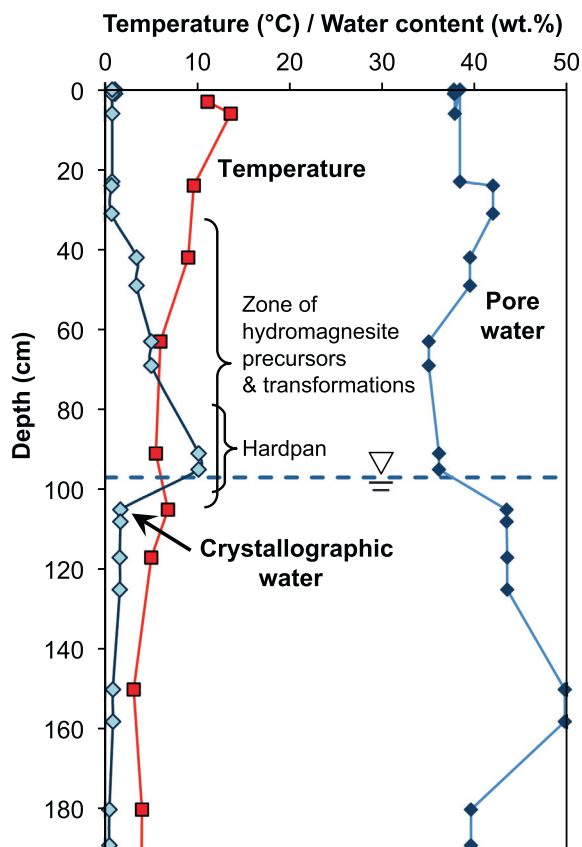


Fig. 3. Temperature profile for profile 4 in July. Sediment and crystallographic water contents were determined gravimetrically by drying sediments at room temperature and then 105 °C. At 105 °C, crystallographic water is only removed from lansfordite, nesquehonite, and dypingite; thus, delineating a zone of hydromagnesite precursors.

cemented sediments also containing nesquehonite and hydromagnesite (Fig. 4a and b). Heating (105 °C) of dry, fresh sediments near the water table resulted in substantial crystallographic water loss near and above the water table (Fig. 3).

As observed using SEM, sediments near the water table exhibited a greater variety of mineral species and crystal morphologies relative to sediments from above or below the water table. Lansfordite crystals appeared dehydrated with desiccation cracks, and long, prismatic crystals of nesquehonite were observed (Fig. 4c). Although dypingite was not detected by XRD, its presence was suggested from the observation of flakey rosettes of Mg-carbonate, a morphology common of dypingite (Fig. 4d; Raade, 1970; Canterford et al., 1984; Power et al., 2007; Power et al., 2009). Rosettes of hydromagnesite plates, a unique crystal morphology, were also observed (Fig. 4e). For comparison, hydromagnesite in most of the Mg-carbonate unit is in the form of micrometre-scale plates (~100 nm thick; Fig. 4f).

Magnesite exhibited two distinct crystal morphologies above and below the water table. Magnesite crystals above the water table (Fig. 5) had some rough surfaces and occasionally formed cone-like terraced morphologies (see

Fig. 5b–e). Magnesite crystals were submicrometre to ~5 µm in width with the rhombohedral crystal morphology being more apparent in smaller crystals (arrows in Fig. 5a). Crystals were notably smaller in sediments containing lower magnesite abundance (Fig. 5b; profile 6: 7 wt.%) than in sediments with higher magnesite abundance (Fig. 5c–e; profile 4: ~40 wt.%). In sediment aggregates, magnesite crystals were often observed wedged between hydromagnesite plates (Fig. 5c, e, and f). Magnesite crystals below the water table (Fig. 6) had smoother crystal faces, were blockier in appearance, and lacked the cone-like morphologies seen above the water table. For comparison, see magnesite in Fig. 6a (below water table) versus magnesite in Fig. 5c. Again, magnesite crystal sizes were noticeably larger in sediments with high magnesite abundance (Fig. 6a from profile 4, 33 wt.%) relative to those with low magnesite abundance (Fig. 6b from profile 6, 6 wt.%). Magnesite crystals were found wedged between hydromagnesite plates in sediment aggregates. Below the water table, some hydromagnesite crystals were observed with rough edges suggesting dissolution (Fig. 6c and d); however, this texture was not observed across the playa and was not consistent between samples.

Median magnesite particle size increased exponentially with increasing magnesite abundance in sediments at the surface and those below the water table (Fig. 7a). In contrast, there was no correlation between particle size and magnesite abundance in sediments near the water table. BET surface areas of a nearly pure sample of magnesite (96 wt.%) collected from the North playa and pure hydromagnesite from profile 2 (~80 cm depth) were 5.9 and 9.7 m²/g, respectively.

4.3. Isotopic data

Stable carbon and oxygen isotope data of the bulk Mg-carbonate sediments in the amalgamated mound (Fig. 1c) have previously been reported (Power et al., 2014). In the present study, the stable carbon and oxygen isotopic compositions of hydromagnesite and magnesite were analyzed separately to provide information regarding differences in environmental conditions or reaction pathways during the formation of these minerals. A key observation was that magnesite was consistently depleted in ¹³C and ¹⁸O relative to hydromagnesite (Fig. 8). Hydromagnesite δ¹³C and δ¹⁸O values showed clear decreasing trends from the surface to depths below the water table. The decreases in δ¹³C and δ¹⁸O values were approximately 2–4‰ and 3–6‰ from the surface to depth, respectively (Fig. 9a). Magnesite stable isotopic data do not exhibit clear trends with depth, particularly for δ¹⁸O values (Fig. 9a).

Previous stable isotopic analyses of the playa and Atlin area waters showed prominent trends indicating CO₂ degassing, photosynthesis and evaporation, which causes isotopic enrichment of ¹³C and ¹⁸O in carbonate minerals precipitated from these waters (Fig. 9; Power et al., 2007; Power et al., 2009; Power et al., 2014). Stable carbon and oxygen isotope values for hydromagnesite and magnesite were converted to equivalent δ¹³C values of DIC and δ¹⁸O values of water based on equilibrium fractionation between each mineral and the fluid to facilitate comparison with the Atlin

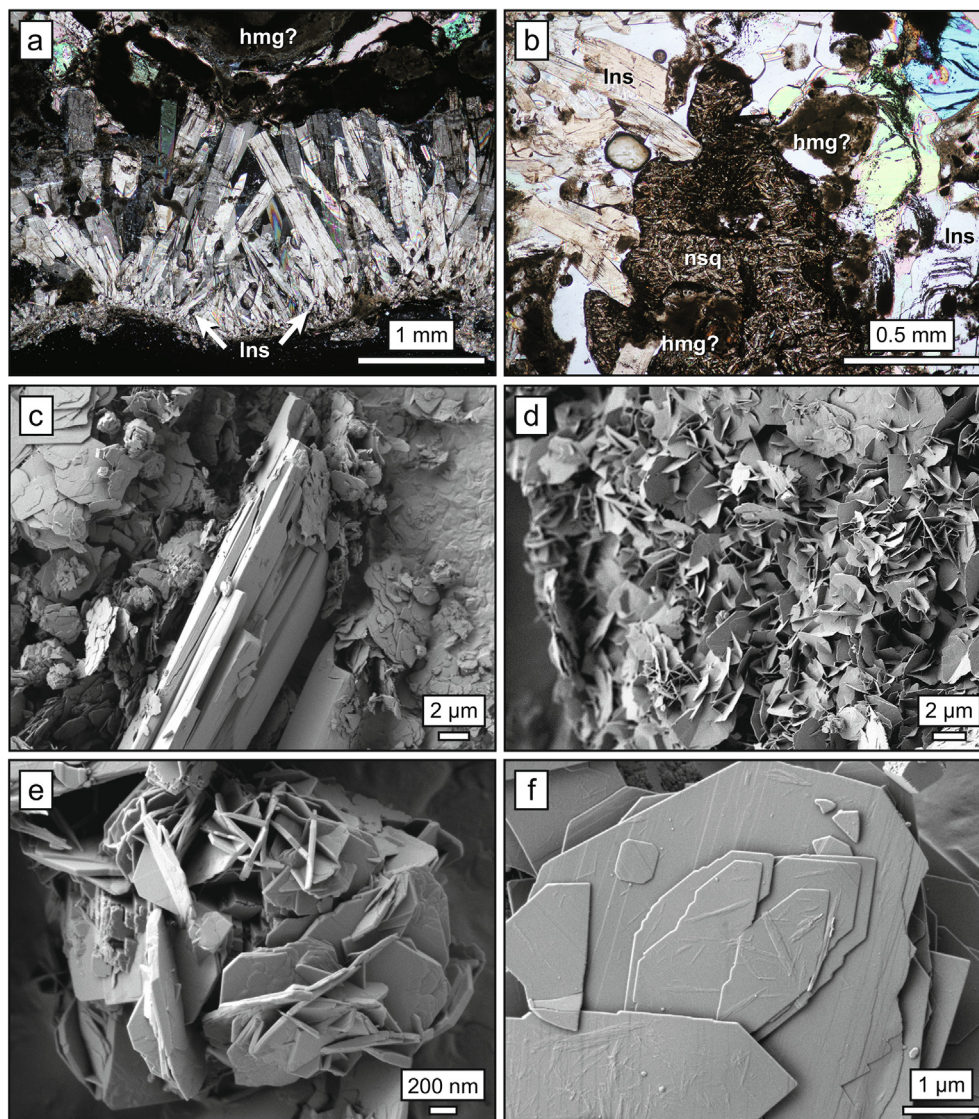


Fig. 4. (a) and (b) Photomicrographs of a hardpan located near the water table at the location of profile 7 (36 wt.% *Ins*). Micrographs show mm-scale lansfordite (*Ins*) crystals cementing sediments that also contain nesquehonite (*nsq*) and hydromagnesite (*hmg*) based on XRD analysis. (c) through (e) Representative scanning electron micrographs of hydrated Mg-carbonate minerals. (c) Elongated crystals of nesquehonite (centre). (d) Flakey, rosette crystal morphology that is most common of dypingite. (e) Rosette crystal arrangement with platelet (~100 nm) crystal morphology indicative of hydromagnesite. Micrographs c, d, and e are of sediments at 91–95 cm depth at profile 4. (f) Typical platy hydromagnesite found throughout the Mg-carbonate sediments (sample from profile 4: 0–5 cm depth).

waters (Fig. 9b). The stable oxygen equilibrium fractionation factor for hydromagnesite (O'Neil and Barnes, 1971), and the stable carbon and oxygen fractionation factors for magnesite (Romanek et al., 1992; Deines, 2004) were used assuming a temperature of 10 °C. The stable carbon equilibrium fractionation factor between DIC and hydromagnesite is not known, and therefore the fractionation factor for dypingite was used, $10^3 \ln \alpha_{\text{dypingite-HCO}_3^-} = 3.8 \pm 1.2\%$ between 20 °C and 25 °C (Wilson et al., 2010). This fractionation factor was adjusted for 10 °C assuming the same temperature dependence as magnesite. Based on this analysis, magnesite precipitated from waters with isotopic compositions ranging from that of groundwater to near-water table isotopic compositions, whereas hydromagnesite

precipitated from waters having isotopic compositions ranging from those of the water table in the mound to surface waters (Fig. 9b). There remains uncertainty regarding the stable carbon and oxygen fractionation factors of hydromagnesite and magnesite.

The determination of exact dates of magnesite formation using radiocarbon analyses is hampered by the numerous potential sources that contribute carbon to groundwater feeding the playa, including soil CO₂, and bedrock carbonate that is radiocarbon dead (e.g., Oskierski et al., 2013). Radiocarbon analyses of magnesite and hydromagnesite from profile 6 (Figs. 8d and 10) showed that near-surface sediments were “younger” (i.e., they contained more ¹⁴C) than deeper sediments. Ground-

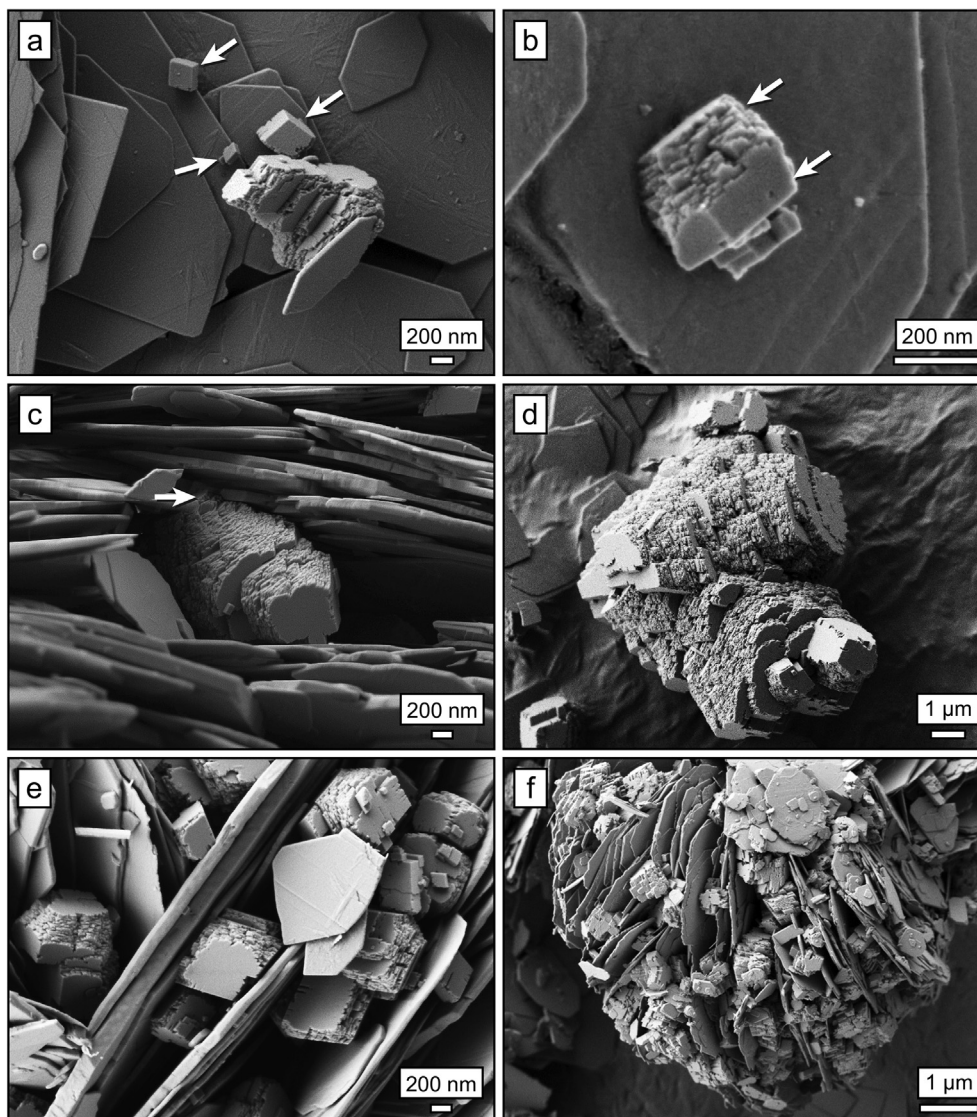


Fig. 5. Representative scanning electron micrographs of magnesite from above water table. (a) A submicron magnesite crystal with a hydromagnesite plate (arrow) attached to the one side (profile 4: 0–5 cm depth, 41 wt.% mgs). Note the presence of three other flat segments or “ledges” on the magnesite that may have held other hydromagnesite plates. Magnesite rhombohedral crystal habits most easily recognized in submicron crystals (arrows). (b) A submicron crystal of magnesite from profile 6 (0–17 cm, 7 wt.% mgs), a low-magnesite profile. (c) A magnesite crystal with a cone-like terraced morphology between a stack of hydromagnesite plates (profile 4: 6–23 cm, 41 wt.% mgs). Note how well the crystal appears to fit (arrow) amongst the hydromagnesite plates. (d) A large (several microns width) aggregate of magnesite crystals showing a rough surface (profile 4: 0–5 cm, 41 wt.% mgs). (e) Sediment aggregate showing magnesite crystals wedged between hydromagnesite plates (profile 4: 24–31 cm, 42 wt.% mgs). (f) Hydromagnesite plates fanned out with magnesite crystals wedged in-between (profile 4: 91–95 cm, 27 wt.% mgs).

water from the nearby well had $\delta^{13}\text{C}_{\text{DIC}}$ and pMC values that indicated mixing between soil DIC, which dominates local spring water, and bedrock carbonate, likely from listwanite (Hansen et al., 2005; Power et al., 2014). Surface and ground waters in the playa had pMC values in the range of 0–12%. For example, water from the main wetland had ~12% modern carbon. Various carbonate sediments associated with playa waters [e.g., pisolite (ara), anoxic wetland sediments (ara), and carbonated benthic mat (ara + dyp)] had radiocarbon ages that indicated formation long before the end of the last glaciation (~11 ka). These ages conflict

with the depositional model that demonstrates that the playas formed post-deglaciation. In contrast, surface samples of nesquehonite and hydromagnesite had pMC values of approximately 70–80%, which may reflect more recent precipitation or exchange of DIC with modern atmospheric CO_2 (Wilson et al., 2009a; Wilson et al., 2014).

5. DISCUSSION

There are two possible pathways for the formation of hydromagnesite and magnesite in the playas: (1) direct pre-

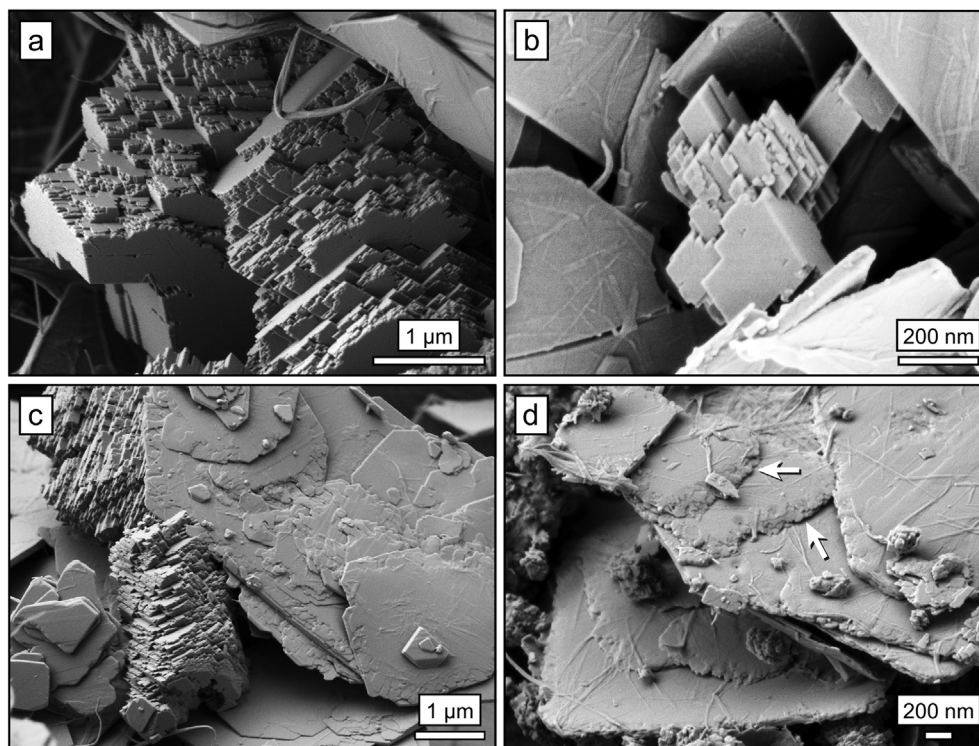
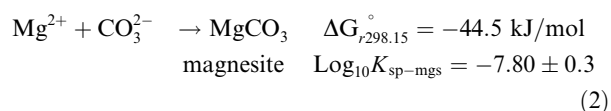
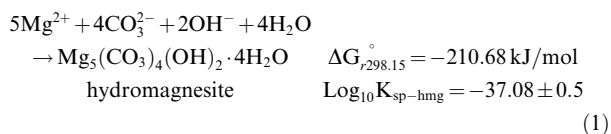


Fig. 6. Representative scanning electron micrographs of magnesite below the water table. (a) The typical rhombohedral crystal morphology of magnesite is more pronounced (profile 4: 117–125 cm depth, 33 wt.% mgs); compare magnesite crystals above the water table (Fig. 5). (b) Magnesite crystals have smoother faces and have a “blockier” appearance in comparison to magnesite above the water table (profile 6: 210–220 cm, 6 wt.% mgs). (c) Magnesite crystals wedge between plates of hydromagnesite that show signs of dissolution (profile 4: 117–125 cm, 33 wt.% mgs). (d) Some hydromagnesite plates with rough plate edges (arrows) indicating dissolution (profile 4: 237–248 cm, 33 wt.% mgs).

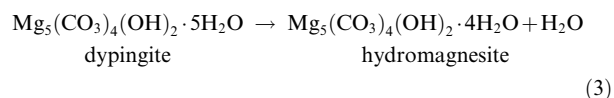
precipitation from pore waters, or (2) mineral transformation. The playas are an open system with a continuous supply of Mg–HCO₃ groundwater that is supersaturated with respect to magnesite at depth, and upon reaching the near-surface becomes saturated with respect to hydromagnesite and other hydrated Mg-carbonate minerals such as lansfordite (Table 2; Power et al., 2014). Therefore, both magnesite and hydromagnesite could precipitate from pore waters within the playa (Eqs. (1) and (2); Shock and Helgeson, 1988; Königsberger et al., 1999; Bénézech et al., 2011; Gautier et al., 2014).



Although lansfordite and nesquehonite precipitate rapidly from aqueous solution (Davies and Bubela, 1973; Hänchen et al., 2008; Hopkinson et al., 2008; Hopkinson et al., 2012), formation of magnesite and hydromagnesite are, to varying degrees, kinetically controlled at Earth’s surface conditions (Königsberger et al., 1999). Specifically,

hydromagnesite precipitation is typically kinetically controlled at temperatures <40 °C; whereas magnesite precipitation is kinetically controlled at <60 °C (Königsberger et al., 1999; Hänchen et al., 2008; Gautier et al., 2014).

Ostwald’s rule of phases states that the pathway to the thermodynamically stable mineral (magnesite in the Mg-carbonate system) passes consecutively through each less stable phase in order of increasing stability (De Yoreo and Vekilov, 2003). Thus, the following transformations would be expected to occur in the Atlin playas: lansfordite → nesquehonite → dypingite → hydromagnesite → magnesite (Königsberger et al., 1999). Some of these transformations have been documented in low-temperature laboratory experiments. For example, nesquehonite transforming to dypingite and then to hydromagnesite at room temperature (e.g., Eq. (3); Hopkinson et al., 2008; Hopkinson et al., 2012; Harrison et al., 2015, 2016; Power et al., 2016; Harrison et al., 2019).



Ruiz-Agudo et al. (2014) state that there are two main mechanisms of mineral transformation. One mechanism is *interface-coupled dissolution-precipitation* whereby an aqueous fluid induces dissolution of one phase to produce an

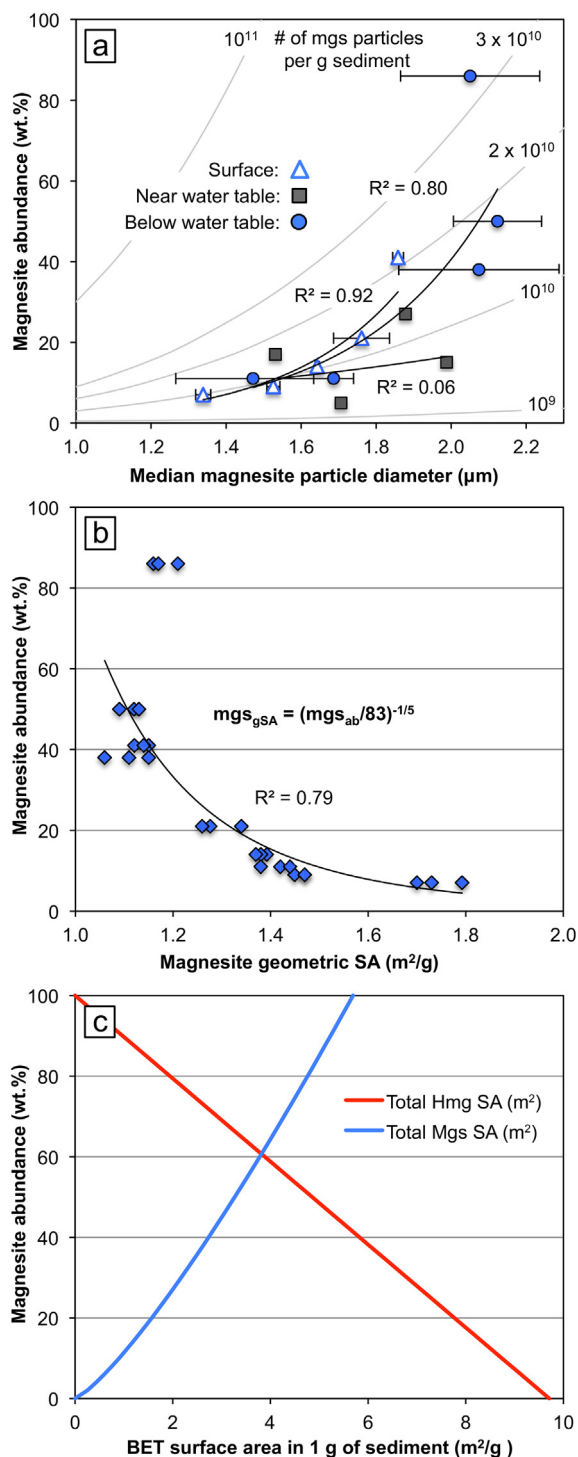
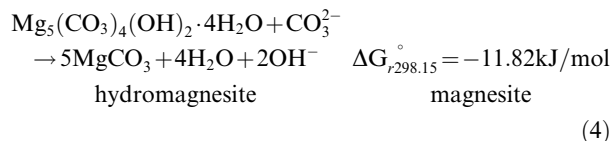


Fig. 7. Magnesian particle size data. (a) Magnesian abundance (wt.%) versus median particle diameter (μm) for magnesian from surface (triangles), near water table (squares), and below water table (circles) sediments. Points represent triplicate analyses with 1 σ standard deviation error bars. Lines of an equal number of particles per gram of sediment are displayed for comparison. (b) Magnesian abundance (wt.%) versus geometric surface area (m²/g). (c) Magnesian abundance (wt.%) versus total surface areas of hydromagnesite (hmg) and magnesite (mgs) in 1 g of Mg-carbonate sediment.

interfacial layer that is supersaturated with respect to other phases. This reacting fluid is undersaturated with respect to the parent solid to initiate its dissolution and the product mineral may take on the crystal morphology of the parent, i.e., a pseudomorphic replacement (e.g., Pedrosa et al., 2017). A second mechanism is when a parent solid-exchanges atoms through diffusion to form another phase in a *solid-state transformation* that may also preserve morphologies. This transformation might involve hydromagnesite dehydrating to form magnesite through a solid-state transformation (Eq. (4); Wagman et al., 1982; Zhang et al., 2000; Di Lorenzo et al., 2014; Gautier et al., 2014).



The transformation of hydromagnesite to magnesite can be achieved within hours in high-temperature (e.g., 110–200 °C) batch experiments, but is estimated to require 10–100 s of years at near-surface conditions (Zhang et al., 2000). In batch experiments (120, 150 and 180 °C) conducted by Di Lorenzo et al. (2014), the conversion of hydromagnesite to magnesite occurred via a dissolution-precipitation process with other transformation mechanisms being excluded based on the experimental data. These high-temperature batch experiments were closed systems and are not necessarily good representations of the playas. The playas form under Earth surface temperatures and are an open system with a continuous supply of Mg–HCO₃ groundwater that, upon evaporation and degassing, is saturated with respect to hydromagnesite. There remain many questions regarding the formation pathways and rates of hydromagnesite and magnesite at Earth's surface given their slow precipitation rates, the complexity of the Mg-carbonate system, and the challenges of studying mineral transformation processes. In particular, it is unclear if mineral transformation processes play an important role in magnesite formation in low-temperature environments such as the Atlin playas, or if magnesite precipitates directly from solution without requiring a hydromagnesite precursor. In the following sections, we assess the precipitation pathways, controls, and rates of hydromagnesite and magnesite formation in the Atlin playas.

5.1. Hydromagnesite formation

5.1.1. Hydromagnesite precipitation pathways

To date, there is no experimental study demonstrating direct nucleation and precipitation of hydromagnesite at Earth surface temperatures from an aqueous solution that is free of any solids, but rather numerous studies showing that it forms from precursor minerals (e.g., Davies and Bubela, 1973; Hopkinson et al., 2012).

The presence of nearly pure hydromagnesite sediments in localized mounds and highly variable abundances of magnesite (below detection to 86 wt.% by XRD) in the amalgamated mound strongly indicates that most of the hydromagnesite is deposited before magnesite formation

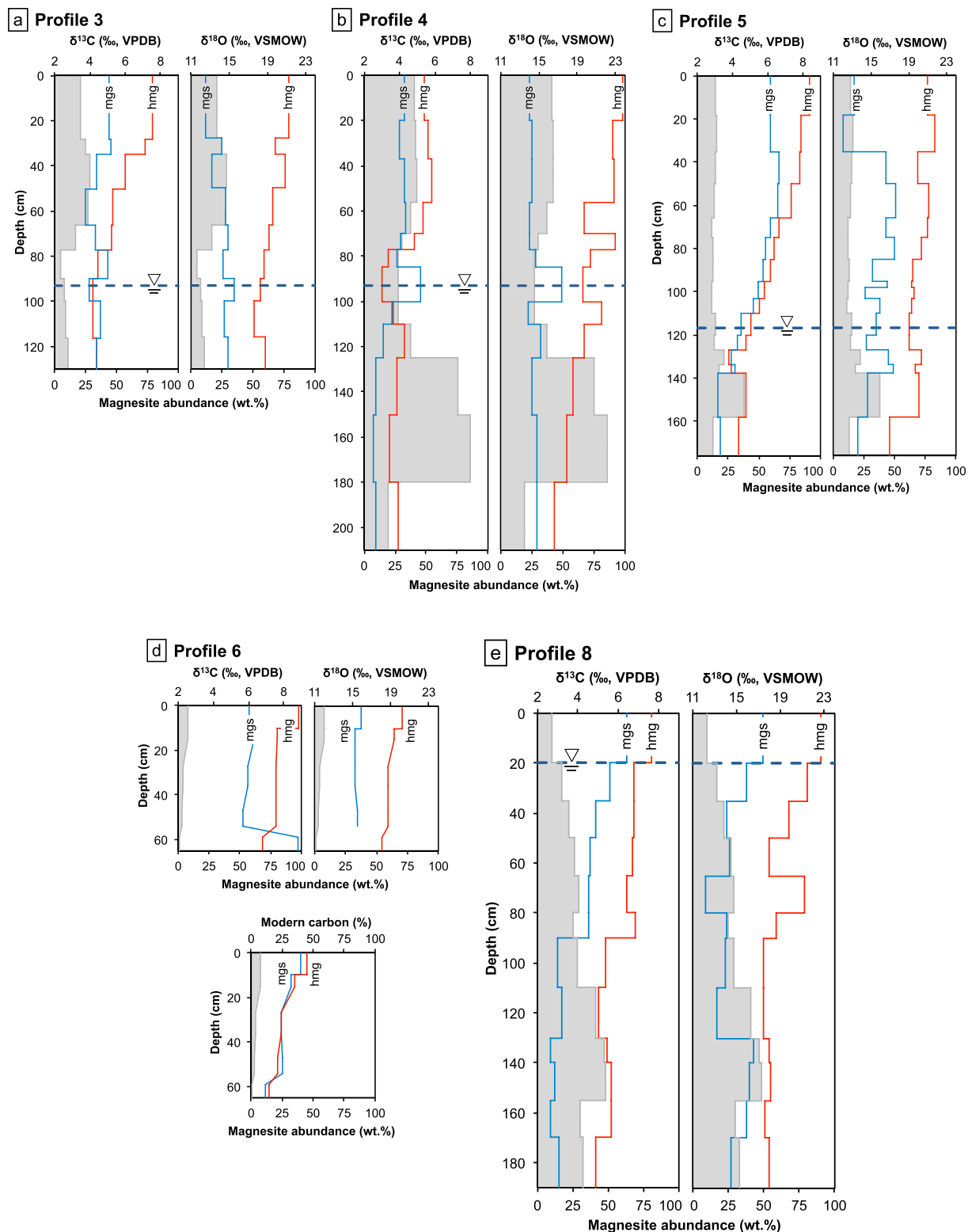


Fig. 8. Plots of depth (cm) versus $\delta^{13}\text{C}$ and $\delta^{18}\text{O}$ values (‰) of hydromagnesite (red line) and magnesite (blue line) from Mg-carbonate sediments from profiles 3 (a), 4 (b), 5 (c), 6 (d) and 8 (e). Also plotted are the positions of the water table (dashed line) and magnesite abundance on the secondary x-axis. (For interpretation of the references to color in this figure legend, the reader is referred to the web version of this article.)

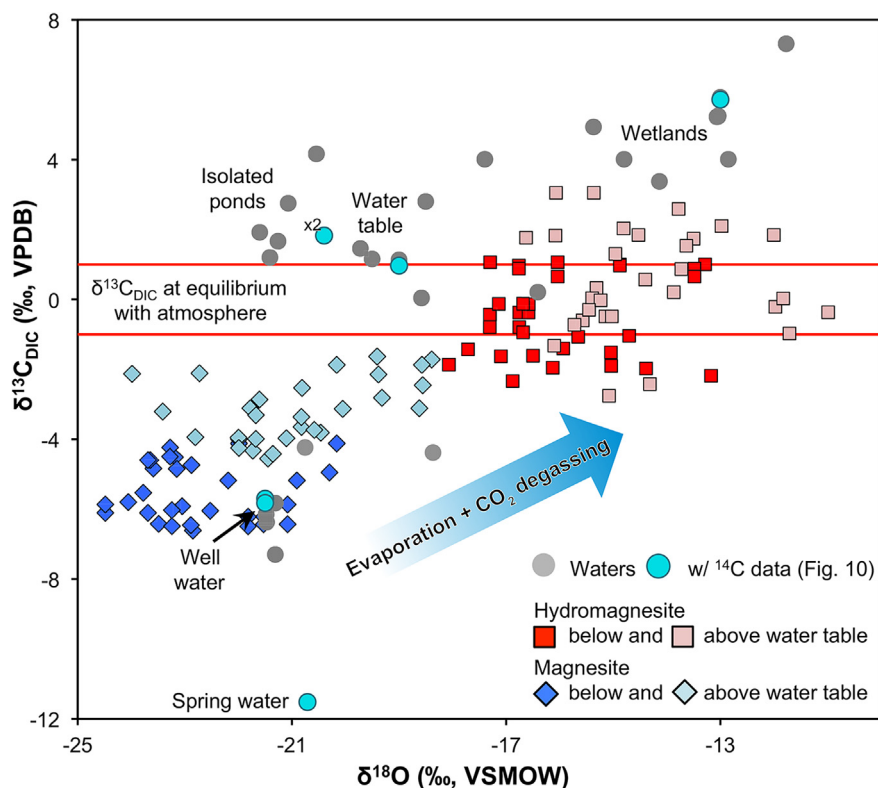


Fig. 9. A plot of estimated $\delta^{13}\text{C}_{\text{DIC}}$ and $\delta^{18}\text{O}$ values of waters from which hydromagnesite and magnesite may have formed from based on equilibrium fractionation. Carbon and oxygen isotopic compositions of the waters collected from the Atlin site are plotted for comparison (Power et al., 2014; Power et al., 2009).

(Fig. 2; Power et al., 2009). Two crystal morphologies of hydromagnesite exist in the playa: (1) a flakey/rosette crystal morphology that is more closely associated with the water table (Fig. 4d and e) and (2) a platy crystal morphology that the vast majority of the hydromagnesite is present as in the playas (Fig. 4f). These two morphologies may represent two stages along a single formation pathway (e.g., a mineral transformation from more hydrated phases; Eq. (3)) or separate pathways (e.g., mineral transformation versus direct precipitation from aqueous solution; Eq. (1)).

The abundance of lansfordite within the hardpan near the water table in the amalgamated mounds is explained by the water chemistry. Here, waters are slightly supersaturated (avg. SI = 0.4) with respect to lansfordite, which is the most hydrated and least stable Mg-carbonate mineral. Lansfordite will readily precipitate from Mg-HCO₃ waters at temperatures <10 °C (Ming and Franklin, 1985). Furthermore, hydromagnesite is at equilibrium in these waters. These findings indicate that hydrated Mg-carbonate precipitation is controlling water chemistry within the mounds.

The mineralogical and textural evidence from sediments collected near the water table (particularly the hardpan) suggests that numerous mineral transformations are occurring at this location. These transformations are consistent with previous studies showing that lansfordite will dehydrate to less hydrated Mg-carbonate phases such as nesquehonite (Ming and Franklin, 1985; Königsberger et al., 1999; Montes-Hernandez and Renard, 2016), which will in turn

readily transform to hydromagnesite (Davies and Bubela, 1973; Hopkinson et al., 2008). Gravimetric analyses of samples collected near the water table further emphasize the unique mineralogical composition of this zone within the Mg-carbonate unit. Heating of fresh sediments from profile 4 to 105 °C delineated a zone containing the more hydrated hydromagnesite precursor minerals, lansfordite, nesquehonite, and dypingite as well as amorphous phases, which were not all captured with XRD (Fig. 3).

Dypingite and unnamed dypingite-like phases are intermediates in the conversion of nesquehonite to hydromagnesite (Hopkinson et al., 2008; Hopkinson et al., 2012). The formation of flakey dypingite on surfaces of nesquehonite has been previously observed, with this morphology maturing into more plate-like forms over time as dypingite transforms to hydromagnesite (Harrison et al., 2013; Power et al., 2016). These textures observed in controlled experiments are similar to those seen in sediments near the water table (Fig. 4) where these transformations are likely occurring through coupled dissolution-precipitation within interfacial waters at mineral surfaces (Power et al., 2016; Power et al., 2017a). The more common platy hydromagnesite (Fig. 4f) likely develops through continued precipitation over time as these crystals tend to be larger and more crystalline than the flakey form. These mineral transformations and morphological changes are consistent with Ostwald step rule and ripening, whereby the latter results in “grain coarsening” or larger well-formed crystals (Morse and

Casey, 1988). Consequently, there is textural evidence indicating that hydromagnesite forms through transformation of more hydrated phases and continues to precipitate from pore waters. However, direct nucleation and precipitation from pore waters versus continued precipitation after a mineral transformation cannot be distinguished from these textures. Furthermore, the kinetics of Mg-carbonate transformations in natural environments remains unclear. In the case of the playas, the transformation of more hydrated phases to hydromagnesite may enable it to by-pass nucleation and hasten its formation.

5.1.2. Hydromagnesite sediment deposition

Mg-carbonate, mainly hydromagnesite, has been deposited in the playa at a rate of between 0.3 and 0.4 mm/yr for approximately 8000 years based on the thickness of this unit and radiocarbon dating of organics at the top of the Ca-Mg-carbonate unit (Fig. 2). This equates to approximately 200–300 g of hydromagnesite deposited per year per square metre with a porosity of 66% as was determined for the playa sediments. Hydromagnesite precipitation rates measured in the laboratory (Gautier et al., 2014) are too fast to account for the age and thickness of the hydromagnesite mounds. For example, the deposition of a metre-scale thickness of hydromagnesite sediments would require only decades based on the measured BET surface area (9.7 m²/g) and laboratory-measured hydromagnesite growth rates (Gautier et al., 2014).

The groundwater that discharges into the playas is undersaturated with respect to hydromagnesite and then becomes saturated upon evaporating and degassing. Waters at the water table undergo an evaporative loss of ~13% of annual precipitation (Power et al., 2014) and are at near equilibrium with respect to hydromagnesite (Table 2). Hydromagnesite precipitation must match that of evapoconcentration to maintain this condition, and is thus effectively transport-controlled. Simply stated, increasing or decreasing evapoconcentration from the playa would lead to proportional changes in hydrated Mg-carbonate deposition rates. This control on formation rate differs from reaction-controlled, which is commonly the regime under which laboratory experiments are conducted to determine mineral dissolution and precipitation rates (Saldi et al., 2009; Saldi et al., 2012; Thom et al., 2013; Gautier et al., 2014).

The precipitation of various hydrated Mg-carbonate minerals and their transformations result in mounds (m-scale) containing mainly hydromagnesite with a platy crystal morphology. The formation of these minerals is mainly driven by CO₂ degassing and evaporation, the latter controlling the precipitation and deposition rates.

5.2. Magnesite formation

5.2.1. Magnesite precipitation pathways

While hydromagnesite exhibits textures that may indicate both mineral transformation (flakey) and precipitation from aqueous solution (platy), magnesite textures suggest only direct precipitation. Magnesite appears spatially separate from hydromagnesite and tends to wedge between

hydromagnesite plates suggesting it does not form at the expense of hydromagnesite, i.e., a mineral transformation. For comparison, magnesite that formed from the transformation of hydromagnesite in high-temperature experiments appeared to have grown from aggregates of hydromagnesite crystals (Di Lorenzo et al., 2014). In the playa sediments, there was no indication of the intergrowth of magnesite and hydromagnesite that would support a mineral transformation process being a dominant pathway for magnesite formation; however, this observation does not preclude the possibility that the initial formation of magnesite occurred via hydromagnesite dehydration at a scale that is not observable by SEM. Mineral transformation reactions can result in a pseudomorphic replacement (Ruiz-Agudo et al., 2014; Pedrosa et al., 2016, 2017), but this is not the case with magnesite and hydromagnesite that have very distinct crystal structures and morphologies (Figs. 4–6). Furthermore, magnesite crystals exhibit growth textures (e.g., spiral crystal growth) demonstrating that these are growing from pore waters.

Equilibrium isotopic fractionation during precipitation of hydromagnesite and magnesite from the same water would produce magnesite that is isotopically enriched in ¹³C and ¹⁸O relative to hydromagnesite, whereas isotopic data shows a depletion (Fig. 8). Clumped isotope geothermometry of magnesite collected from near the surface of profile 4 gave a formation temperature in the range of 1–11 °C (Falk and Kelemen, 2015 and references therein), which is consistent with the measured temperature range for the modern playa from the surface to 2 m depth (Fig. 3). Thus, magnesite precipitating from a much higher temperature cannot account for its ¹³C and ¹⁸O depletions relative to hydromagnesite.

Although magnesite is intermixed amongst hydromagnesite, its isotopic depletion relative to hydromagnesite may be due to these minerals having formed in spatially distinct environments: near-surface in the case of hydromagnesite and shallow subsurface in the case of magnesite. Hydromagnesite δ¹³C and δ¹⁸O values increased towards the surface (Fig. 8) indicating its formation was likely driven by evaporation and CO₂ degassing nearer to the surface (Fig. 9). In contrast, magnesite does not exhibit clear trends in δ¹³C and δ¹⁸O values with depth and has an isotopic signature suggesting precipitation from groundwater assuming equilibrium fractionation (Fig. 9). This spatial separation is achieved as the mound grows larger, i.e., more sediment is deposited, and the Mg-carbonate unit becomes thicker, which occurs over 1000 s of years. Thus, the isotopic signatures imply that magnesite formation must have started later after the majority of hydromagnesite had been deposited to form the mound. This hypothesis is consistent with the mineralogical data that show there being mounds of nearly pure hydromagnesite sediment. This does not mean that hydromagnesite is not continuing to precipitate from deeper waters, but its precipitation is insufficient to completely overprint the isotopic signal that was developed as the mounds were deposited. It is expected that magnesite is forming in isotopic equilibrium from pore waters as the rate of formation is very slow; whereas kinetic isotope effects during CO₂ degassing and evaporation could lead

to enrichment in ^{13}C and ^{18}O compositions of hydromagnesite (Hendy, 1971; Clark and Fritz, 1997). These hypotheses are consistent with the isotope data (Fig. 8). Kinetic fractionation during carbonate precipitation from highly alkaline waters can lead to lighter isotope values (Wilson et al., 2010; Sade and Halevy, 2017); however, it is unclear if this is occurring in the playas.

Radiocarbon dating of organics at the top of the Ca-Mg-carbonate unit showed that the Mg-carbonate unit is almost 8000 years old, whereas radiocarbon analyses of playa carbonates and modern waters showed these being considerably older (Fig. 10). Because the playa cannot be older than ~ 11 ka, the pMC values for the carbonate sediments must reflect the incorporation of older carbon sourced from listwanite. Some sediments in association with the main wetland (e.g., nesquehonite surface crust) had greater pMC values

than modern source waters from which they may have precipitated from, suggesting pMC values are dictated by the degree of CO_2 exchange with the atmosphere rather than actual age. Furthermore, surface waters had greater pMC values (e.g., 11.7%) than groundwater (e.g., 10.7%; Fig. 10). As with the stable isotopic compositions, magnesite usually had lower pMC values in comparison to hydromagnesite (Fig. 8d), further indicating its formation at depth as opposed to a more near-surface deposition for hydromagnesite.

There is no evidence of extensive hydromagnesite dissolution and pore waters in the unsaturated zone are saturated with respect to hydromagnesite. The textural and isotopic data indicate that magnesite precipitation from solution occurs from a fluid of a different isotopic composition than hydromagnesite, thus indicating that they mainly formed at different times.

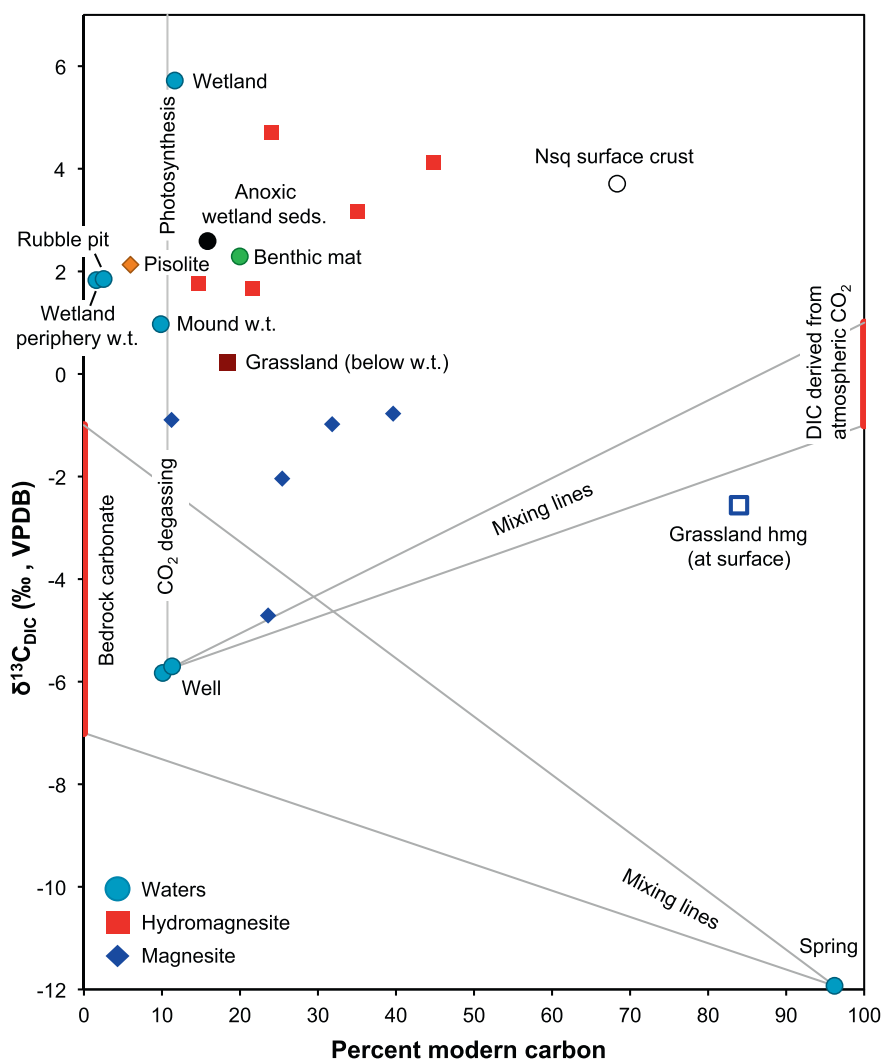


Fig. 10. Stable carbon ($\delta^{13}\text{C}$) and percent modern carbon (pMC) data for secondary carbonates [e.g., nesquehonite (nsq), hydromagnesite (hmg), and magnesite (mgs)] from the playas and waters from the Atlin area. The anoxic wetland sediments and pisolite were primarily composed of aragonite, the benthic mat contained aragonite and dypingite, and the grassland sediments below the water table contained aragonite and ankerite/disordered dolomite. Measurement errors are typically smaller than the symbols used. Fields for bedrock carbonate (Hansen et al., 2005) and DIC in equilibrium with CO_2 (Mook et al., 1974) are also shown.

5.2.2. Trends in magnesite abundance

The relative abundance of magnesite depends on the relative changes in hydrated Mg-carbonate mineral abundances, magnesite formation rate, and the age of the sediments, all of which are difficult to determine with absolute certainty. In the Mg-carbonate unit, magnesite abundance ranges substantially both laterally and with depth (Fig. 2). Noteworthy are the lower magnesite abundances near the water table that are likely due to pervasive precipitation of hydrated Mg-carbonate minerals, such as lansfordite, that “dilute” magnesite (see in profiles 3, 4, 6, and 7 in Fig. 2). This explanation is supported by the particle size data that showed no correlation between magnesite abundance and median particle diameter, which would occur if magnesite abundance was diluted by extensive precipitation of hydrated Mg-carbonate (Fig. 7a).

A variable precipitation rate with depth could explain why most profiles have magnesite abundances in near-surface sediments that are similar to those in sediments that are much deeper and older (Fig. 2). Profiles 4 and 8 are the only ones that show a modest positive correlation between magnesite abundance and depth. At and above the water table, evaporation and CO₂ degassing increase the saturation of Mg-carbonate minerals. The Mg-carbonate sediments had a pH of 9 at the surface versus ~8 at the water table. Thus, it is expected that the rate of magnesite precipitation is faster above the water table than below because its formation rate is faster at higher pH values (Saldi et al., 2009; Saldi et al., 2012). The differences between magnesite crystal morphologies above and below the water table (Figs. 5 and 6) may reflect different precipitation mechanisms and rates (Schott et al., 2012; Berninger et al., 2016). The formation of cone-like terraced morphologies (spiral crystal growth; Fig. 5b–e) above the water table indicates that new layers are generated in a shorter time than that required for a layer to extend to the crystal edge; thus, each new layer is smaller than the previous one. As with precipitation rate, layer generation frequency increases with increasing saturation with respect to magnesite (Schott et al., 2012), which further suggests that pore waters in the unsaturated zone are more supersaturated with respect to magnesite than those below the water table where crystals are comparatively smooth (2D crystal growth; Fig. 6a and b). Consequently, the mineralogical and textural evidence suggests that there is likely a range of magnesite formation rates given the lack of a consistent positive correlation between magnesite abundance and depth.

5.3. Quantifying magnesite formation rates

Rates of magnesite precipitation at Earth’s surface conditions have only been estimated from high-temperature experiments (e.g., Saldi et al., 2009; Saldi et al., 2012). Here, we use mineralogical, particle size, and surface area data to determine magnesite formation rates that can account for the magnesite abundances measured in the Atlin playa sediments that have formed since the last deglaciation (~11 ka).

Mineral surface area is needed to calculate precipitation rates (e.g., Saldi et al., 2009; Saldi et al., 2012; Gautier et al.,

2014). A direct BET measurement of magnesite surface area is not possible because hydromagnesite is present. In addition, magnesite surface area will evolve as it forms over time. As a starting point, the relationship between geometric surface area (mgs_{gSA}) and magnesite abundance (mgs_{ab}) was determined using magnesite particle size distributions assuming cubic particles (Fig. 7b). For example, a nearly pure magnesite sample (96 wt.%) collected from the North playa would have a geometric surface area of 0.97 m²/g based on its particle size distribution; however, its BET surface area was 5.9 m²/g. This sample was used to calculate a surface roughness factor of 6.1, which is defined as the ratio of the BET surface area divided by the geometric surface area (Brantley and Lebedeva, 2011). The assumption is that all magnesite in the playas has the same surface roughness. In Equation (5), the geometric surface area (Fig. 7b) is multiplied by this surface roughness factor to give a calculated specific surface (mgs_{SA} ; m²/g) based on magnesite abundance (mgs_{ab} ; wt.%) for samples for which BET surface area was not measured directly.

$$mgs_{SA} = 6.1 \cdot \left(\frac{mgs_{ab}}{83} \right)^{-1/5} \quad (5)$$

To calculate the magnesite formation rate, its specific surface area (mgs_{SA}) was updated based on its abundance (wt.%). Moles of magnesite (mol_{mgs}) were calculated using Equation (6):

$$mol_{mgs} = k \cdot mgs_{SA} \cdot m_{mgs} \cdot t \quad (6)$$

where k is the rate constant (mol/cm²/s), mgs_{SA} is the calculated magnesite specific surface area (converted to cm²/g; Eq. (5)), m_{mgs} is the cumulative magnesite mass (g), and t is the time interval (s). The initial mass of magnesite used in the calculation was equal to a single 100 nm crystal of magnesite, which is likely to be equal or larger than the critical nucleus size (De Yoreo and Vekilov, 2003). The maximum calculated specific surface area was limited to 20 m²/g, which is equivalent to all magnesite being present as 100 nm cubes. Magnesite abundances were cumulated each year for 8000 years, the oldest radiocarbon date of organics from profile 6 (Eq. (7)):

$$m_{mgs} = M_{mgs} \sum_{i=0}^n mol_{mgs}(i) \quad (7)$$

where M_{mgs} is the molar mass of magnesite used to calculate the cumulative mass of magnesite based on the cumulative moles of magnesite for a given year (i). Specific surface area (Eq. (5)) was updated based on the magnesite abundance (Eq. (8)). A hydromagnesite deposition rate of 270 g per year per square meter was used. This deposition rate was calculated based on the thickness of the Mg-carbonate unit and radiocarbon dating of buried vegetation. The magnesite abundance (mgs_{ab}) was calculated using Equation (8).

$$mgs_{ab} = \frac{m_{mgs}}{(m_{mgs} + m_{hmg})} \cdot 100\% \quad (8)$$

where m_{mgs} and m_{hmg} are the masses of magnesite and hydromagnesite, respectively. A rate constant of between 10⁻¹⁷ and 10⁻¹⁶ mol/cm²/s is needed to obtain the range

of magnesite abundances in the Atlin playas given the estimated ages of the Mg-carbonate sediments (Fig. 12). Increasing the initial number of nuclei or mass of magnesite shifts the curves to younger ages. Adjusting the surface roughness factor changes the slope of the exponential increase (e.g., a shallower slope with a lower surface roughness factor). Depending on the rate of magnesite formation, the hydromagnesite deposition rate allowed for a buildup of between 30 and 300 cm of hydromagnesite sediments before a detectable amount (~1% by XRD) of magnesite would have formed in 100–1000 s of years. This deposition of hydromagnesite prior to magnesite formation fits the depositional model (Power et al., 2014) and isotopic evidence.

It is also worth noting the changes in the total surface area between hydromagnesite and magnesite in a fixed mass of sediment. As the relative abundance of hydromagnesite decreases and magnesite increases, the total magnesite surface area increases despite a decreasing specific surface area due to an increase in median crystal size (Fig. 7c). Consequently, there is positive feedback between increasing magnesite abundance and its total surface area, which is the reason for the exponential increase in magnesite abundance and may explain the lateral variation in magnesite abundance in the amalgamated mound (Fig. 2). Because of the exponential rise in magnesite abundance (Fig. 12a) little time is needed to shift from comparatively low magnesite abundances (e.g., profiles 1, 2, 6 and 7) to relatively high magnesite abundances (e.g., profiles 3, 4, 5 and 8). This is an important finding as the lateral variation in magnesite abundance (Fig. 2) cannot be explained by variable precipitation rates as the water chemistry at the water table is consistent across the mound even though the magnesite abundances widely vary, e.g., 27 wt.% at profile 4, and 1 wt.% at profiles 6 and 7. Thus, variable sediment ages may account for the lateral differences in magnesite abundances. For instance, aerial photographs (Fig. 1b and c) of the playas show numerous metre-scale localized mounds demonstrating irregular, non-uniform rates of sediment deposition that suggests there could be some lateral variation in sediment age. Continued deposition of these localized mounds causes them to amalgamate into larger mounds, including the one sampled in this study (Fig. 1c). As such, these smaller mounds are no longer distinguishable, and any record of lateral variation in sediment age is lost.

5.4. Relative rates of hydromagnesite and magnesite formation

The relative rates of hydromagnesite and magnesite formation are an interesting conundrum. The mineralogical, textural and stable isotopic data demonstrate that hydromagnesite is mostly deposited first with magnesite forming later, thereby necessitating that hydromagnesite initially forms faster than magnesite. In order for magnesite abundance to increase, its rate must later become faster than that of hydromagnesite. The exception would be if hydromagnesite were dissolving or transforming to magnesite, which the data do not support, particularly when considering that

pore waters at the water table are saturated with respect to both minerals. The following discusses induction times, precipitation rates, and transport as factors that would allow the relative abundance of magnesite to increase over time.

Induction time is the time required for nucleation and formation of a detectable amount of the crystalline phase from the initial moment a solution becomes supersaturated and is strongly dependent on the saturation state (De Yoreo and Vekilov, 2003; Kashchiev and van Rosmalen, 2003; De Yoreo et al., 2013). For example, nesquehonite has an induction time of <1 and 600 min with saturation ratios of 1.15 and 1.07, respectively (Hänchen et al., 2008). In batch reactors that converted hydromagnesite to magnesite at elevated temperatures (110, 150 and 200 °C), Zhang et al. (2000) estimated an induction time of 18–200 years at 25 °C followed by “half-lives” of hydromagnesite of 4.7 or 73 years depending on solution chemistry. Particle size data support magnesite formation being nucleation-limited as magnesite abundance mainly increases through crystal growth rather than nucleation of more crystals (Fig. 7a; Giammar et al., 2005; Swanson et al., 2014). For example, an increase in magnesite abundance from 5 to 90 wt.% requires an increase in median particle diameter from approximately 1.2–1.3 µm to 2.0–2.2 µm, yet only a 3-fold increase in the number of particles (Fig. 7a). These findings are supported by previous studies indicating that magnesite formation may be nucleation-limited (Giammar et al., 2005) and that seeding experiments with magnesite particles accelerates its formation (Swanson et al., 2014; Felmy et al., 2015). A long induction time may be a contributing factor in delaying magnesite formation, thereby allowing the buildup of hydromagnesite sediments.

Rates of hydromagnesite and magnesite precipitation at 25 °C have been estimated from higher temperature experiments by Gautier et al. (2014) and Saldi et al. (2009, 2012), respectively (Fig. 11). These data show that magnesite growth rates may be faster than hydromagnesite rates at saturation indices above 1.5–2.0 with respect to each mineral. At Atlin, water collected from the water table had average saturation indices for hydromagnesite and magnesite of 0.0 and 2.2, respectively (Fig. 11; Table 2 – profile 4). Although the extrapolation of precipitation rates from high-temperature experiments to low-temperature conditions is fraught with uncertainty, this comparison suggests that the rate of surface-area normalized magnesite growth could be faster than that of hydromagnesite at the observed fluid composition. However, the transformation of more hydrated phases may offer a faster pathway for hydromagnesite formation given that lansfordite and nesquehonite readily precipitate from saturated solutions (Ming and Franklin, 1985; Hänchen et al., 2008). Consequently, a long induction time (i.e., nucleation-limited) for magnesite may be delaying its formation in comparison to hydromagnesite, which may also have the added advantage of forming through mineral transformation processes; however, precipitation rates alone cannot explain the increase in magnesite abundance in the playa.

Transport- versus reaction-controlled regimes are important for interpreting the rates of hydromagnesite and mag-

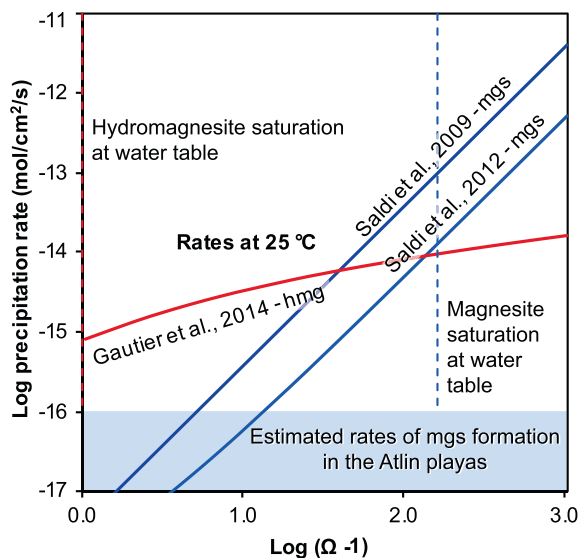


Fig. 11. Hydromagnesite (Gautier et al., 2014) and magnesite growth rates (Saldi et al., 2009; Saldi et al., 2012) as a function of saturation. The vertical dashed lines denote the hydromagnesite and magnesite saturation at the profile 4 water table (Table 2).

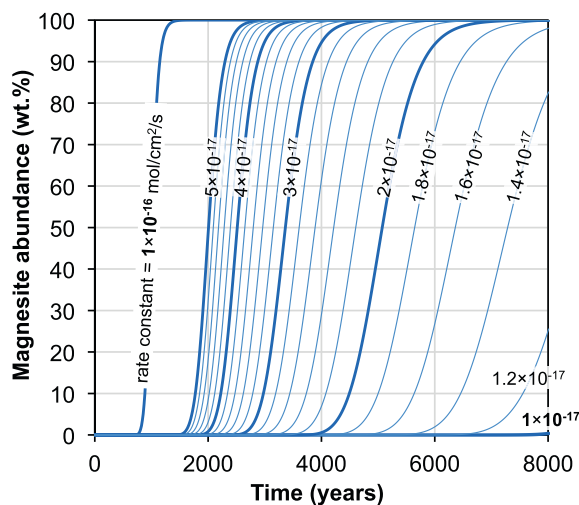


Fig. 12. (a) Calculated magnesite abundances (wt.%) versus time (years) using rate constants from 10^{-17} to 10^{-16} mol/cm²/s.

nesite formation in the Atlin playas. Waters at the water table are in near-equilibrium with respect hydromagnesite, as such hydromagnesite must be precipitating at a rate that matches evapoconcentration and groundwater replenishment of solutes. Thus, hydromagnesite deposition is effectively transport-controlled; whereas magnesite remains supersaturated and its precipitation rate is reaction-controlled and potentially faster than that of hydromagnesite. As a result, the abundance of magnesite could increase over time without the loss of hydromagnesite.

As the abundance and total surface area of magnesite increase (Fig. 7c), its formation may shift from reaction- to transport-controlled. In this scenario, magnesite would precipitate in equilibrium with pore waters and cause pore

waters to become undersaturated with respect to hydromagnesite, thereby causing it to dissolve. This scenario can be considered a mineral transformation process that is occurring at the pore scale, whereby water (i.e., reacting fluid) is undersaturated with one phase, causing dissolution, and saturated with another phase, causing precipitation. In the case of ancient Mg-carbonate deposits, this shift in controlling regime may have led to the loss of hydromagnesite leaving a nearly pure deposit of magnesite (e.g., Melezhik et al., 2001; Alçiçek, 2009).

6. CONCLUSIONS AND IMPLICATIONS

The hydromagnesite–magnesite playas near Atlin, British Columbia are a dynamic environment that affords a unique opportunity to study low-temperature Mg-carbonate mineral formation that has occurred over millennia. Groundwaters are supersaturated with respect to magnesite and become saturated with respect to lansfordite and hydromagnesite through evaporation and CO₂ degassing in the playas. Hydromagnesite likely forms through the transformation of more hydrated phases (e.g., lansfordite) and continued precipitation from pore waters, whereas magnesite does not appear to form at the expense of hydromagnesite, but rather as a separate precipitate from pore waters. The isotopic composition of magnesite is distinct from hydromagnesite and supports that magnesite has largely formed after hydromagnesite at depth from waters that are isotopically light in comparison to those that formed most of the hydromagnesite. Thus, magnesite formation and the increase in its abundance over time cannot be explained by the transformation of hydromagnesite to magnesite.

The formation of hydromagnesite precursors such as lansfordite and nesquehonite that readily precipitate from saturated solutions is dictated by evapoconcentration and replenishment of groundwater. Thus, transport is rate-limiting rather than precipitation rates of these precursors and possibly even the transformation to hydromagnesite. These mineral transformations have led to substantial deposition of hydromagnesite despite its formation being kinetic controlled at low temperature. With hydrated Mg-carbonate minerals controlling pore water chemistry, magnesite is kept highly supersaturated and is thus reaction-controlled, allowing the abundance of magnesite to increase over time. Magnesite formation rates in the range of 10^{-17} to 10^{-16} mol/cm²/s account for the measured magnesite abundances in the playas over the estimated sediment ages. Our study provides the first magnesite formation rate determined using field data and is applicable to understanding magnesite formation along with hydromagnesite in modern and ancient sedimentary environments that have been studied globally (Garber et al., 1990; Fallick et al., 1991; Renault, 1993; Braithwaite and Zedef, 1994; Spotl and Burns, 1994; Coshell et al., 1998; Zedef et al., 2000; Léveillé et al., 2007; Alçiçek, 2009; Kazmierczak et al., 2011; Mees et al., 2011; Last and Last, 2012; Sanz-Montero and Rodríguez-Aranda, 2012; Chagas et al., 2016; del Real et al., 2016; Lin et al., 2017).

The Atlin playas, as a natural analogue for CO₂ sequestration, provide numerous lessons for the long-term storage

of anthropogenic CO₂ within Mg-carbonate minerals at Earth's surface. Hydrated Mg-carbonate minerals such as lansfordite and nesquehonite have fast precipitation rates but require much higher dissolved inorganic carbon and Mg concentrations for their formation in comparison to magnesite. While transformations from less stable to more stable hydrated Mg-carbonates over time produces minerals with better long-term stability, the transformation of hydromagnesite to magnesite appears limited. Instead, magnesite seeding would offer faster formation rates by eliminating induction times. An important consideration is that the playas are an open system with a continuous supply of Mg–HCO₃ groundwater. In a carbon storage scenario, a closed system should be maintained unless waters in an open system are saturated with respect to the minerals being used to store the carbon; otherwise, these will eventually dissolve and possibly release CO₂.

ACKNOWLEDGEMENTS

We acknowledge the support of the Natural Sciences and Engineering Research Council of Canada (NSERC) through a Discovery Grant to G.M. Dipple. Thanks to Kate Carroll for assistance with stable isotope analyses. Great thanks to Jenine McCutcheon and Rick White for their help in the field. We thank Eric Unger and Maria Heissig of Lake Atlin Waterfront Place and Norm Graham and Fionnuala Devine of Discovery Helicopters Ltd. for access to the playas. We appreciate the comments by the reviewers and editor that led to the improvement of our manuscript.

APPENDIX A. SUPPLEMENTARY MATERIAL

Supplementary data to this article can be found online at <https://doi.org/10.1016/j.gca.2019.04.008>.

REFERENCES

- Aitken J. D. (1959) Atlin Map Area, British Columbia. Geological Survey of Canada, Memoir 307, 389 pages and accompanying map at 301:253 440 scale.
- Alıçık H. (2009) Late Miocene nonmarine sedimentation and formation of magnesites in the Acıgol Basin, southwestern Anatolia, Turkey. *Sediment. Geol.* **219**, 115–135.
- Ash C. H. (1994) Origin and tectonic setting of ophiolitic ultramafic and related rocks in the Atlin area, British Columbia (NTS 104N), Bulletin 94, 48 p.
- Ash C. H. (2001) Relationship between ophiolites and gold-quartz veins in the North American Cordillera. British Columbia Department of Energy, Mines and Petroleum Resources, Bulletin 108, 140 p.
- Ash C. H. and Arksey R. L. (1990a) The Atlin ultramafic allochthon: ophiolite basement within the Cache Creek Terrane; tectonic and metallogenic significance (104N/12), Geological Fieldwork 1989. B.C. Department of Energy and Mines, pp. 365–374.
- Ash C. H. and Arksey R. L. (1990b) Tectonic setting of listwanite-gold deposits in the Atlin area, N.W. B.C., NTS (104N/12). Ministry of Energy, Mines and Petroleum Resources, Province of British Columbia.
- Ash C. H., Macdonald R. W. J. and Arksey R. L. (1991) Towards a Deposit Model for Ophiolite Related Mesothermal Gold in British Columbia; Geological Fieldwork, in: BC Department of Energy and Mines, Paper 1992-1, pp. 253–260.
- Barker S. L. L., Dipple G. M., Dong F. and Baer D. S. (2011) Use of laser spectroscopy to measure the ¹³C/¹²C and ¹⁸O/¹⁶O compositions of carbonate minerals. *Anal. Chem.* **83**, 2220–2226.
- Bea S. A., Wilson S. A., Mayer K. U., Dipple G. M., Power I. M. and Gamazo P. (2012) Reactive transport modeling of natural carbon sequestration in ultra-mafic mine tailings. *Vadose Zone J.*, 11.
- Beavan N., Halcrow S., McFadgen B., Hamilton D., Buckley B., Sokha T., Shewan L., Sokha O., Fallon S., Miksic J., Armstrong R., O'Reilly D., Domett K. and Chhem K. R. (2012) Radiocarbon dates from jar and coffin burials of the Cardamom Mountains reveal a unique mortuary ritual in Cambodia's Late- to Post-Angkor Period (15th-17th Centuries AD). *Radiocarbon* **54**, 1–22.
- Beinlich A. and Austrheim H. (2012) In situ sequestration of atmospheric CO₂ at low temperature and surface cracking of serpentinized peridotite in mine shafts. *Chem. Geol.* **332**, 32–44.
- Bénéze P., Saldi G. D., Dandurand J. L. and Schott J. (2011) Experimental determination of the solubility product of magnesite at 50 to 200 °C. *Chem. Geol.* **286**, 21–31.
- Berninger U.-N., Jordan G., Lindner M., Reul A., Schott J. and Oelkers E. H. (2016) On the effect of aqueous Ca on magnesite growth – Insight into trace element inhibition of carbonate mineral precipitation. *Geochim. Cosmochim. Acta* **178**, 195–209.
- Bloodgood M. A., Rees C. J. and Lefebvre D. V. (1989) Geology and mineralization of the Atlin area, northwestern British Columbia (104N/11W and 12E); Geological Fieldwork 1988. B. C. Department of Energy and Mines Paper **1989-1**, 311–322.
- Braithwaite C. J. R. and Zedef V. (1994) Living hydromagnesite stromatolites from Turkey. *Sediment. Geol.* **92**, 1–5.
- Brantley S. L. and Lebedeva M. (2011) Learning to read the chemistry of regolith to understand the critical zone. In Annual Review of Earth and Planetary Sciences (eds. R. Jeanloz, K. H. Freeman), vol. 39, pp. 387–416.
- Bruker (2004) AXS, Topas V.3.0: General Profile and Structural Analysis Software for Powder Diffraction Data. Bruker AXS, Germany. Powder Diffraction.
- Bruker (2008) AXS, DIFFRACplus EVA 14 Release 2008, Karlsruhe, Germany.
- Brunauer S., Emmett P. H. and Teller E. (1938) Adsorption of gases in multimolecular layers. *J. Am. Chem. Soc.* **60**, 309–319.
- Canterford J. H., Tsambourakis G. and Lambert B. (1984) Some observations on the properties of dypingite, Mg₅(CO₃)₄(OH)₂•5H₂O, and related minerals. *Mineral. Mag.* **48**, 437–442.
- Chagas A. A. P., Webb G. E., Burne R. V. and Southam G. (2016) Modern lacustrine microbialites: towards a synthesis of aqueous and carbonate geochemistry and mineralogy. *Earth-Sci. Rev.* **162**, 338–363.
- Christ C. L. and Hostetler P. B. (1970) Studies in the system MgO–SiO₂–CO₂–H₂O (II): the activity-product constant of magnesite. *Am. J. Sci.* **268**, 439–453.
- Clark I. and Fritz P. (1997) *Environmental Isotopes in Hydrogeology*. CRC Press, U.S.A.
- Coshell L., Rosen M. R. and McNamara K. J. (1998) Hydromagnesite replacement of biomineralized aragonite in a new location of Holocene stromatolites, Lake Walyungup, Western Australia. *Sedimentology* **45**, 1005–1018.
- Das Sharma S., Patil D. J. and Gopalan K. (2002) Temperature dependence of oxygen isotope fractionation of CO₂ from magnesite-phosphoric acid reaction. *Ind. Eng. Chem. Res.* **66**, 589–593.
- Davies P. J. and Bubela B. (1973) Transformation of nesquehonite into hydromagnesite. *Chem. Geol.* **12**, 289–300.

- De Yoreo J. J. and Vekilov P. G. (2003) Principles of crystal nucleation and growth. In *Biom mineralization* (eds. P. M. Dove, J. J. DeYoreo and S. Weiner). Mineralogical Soc America, Washington, pp. 57–93.
- De Yoreo J. J., Waychunas G. A., Jun Y. S. and Fernandez-Martinez A. (2013) In situ investigations of carbonate nucleation on mineral and organic surfaces. In *Geochemistry of Geologic CO₂ Sequestration* (eds. D. J. DePaolo, D. R. Cole, A. Navrotsky and I. C. Bourg). Mineralogical Soc Amer, Chantilly, pp. 229–257.
- Deines P. (2004) Carbon isotope effects in carbonate systems. *Geochim. Cosmochim. Acta* **68**, 2659–2679.
- del Real P. G., Maher K., Kluge T., Bird D. K., Brown G. E. and John C. M. (2016) Clumped-isotope thermometry of magnesium carbonates in ultramafic rocks. *Geochim. Cosmochim. Acta* **193**, 222–250.
- Di Lorenzo F., Rodríguez-Galán R. M. and Prieto M. (2014) Kinetics of the solvent-mediated transformation of hydromagnesite into magnesite at different temperatures. *Mineral. Mag.* **78**, 1363–1372.
- Falk E. S. and Kelemen P. B. (2015) Geochemistry and petrology of listvenite in the Samail ophiolite, Sultanate of Oman: complete carbonation of peridotite during ophiolite emplacement. *Geochim. Cosmochim. Acta* **160**, 70–90.
- Fallick A. E., Ilich M. and Russell M. J. (1991) A stable isotope study of the magnesite deposits associated with the alpine-type ultramafic rocks of Yugoslavia. *Econ. Geol.* **86**, 847–861.
- Fallon S. J., Fifield L. K. and Chappell J. M. (2010) The next chapter in radiocarbon dating at the Australian National University: status report on the single stage AMS. *Nucl. Instr. Methods Phys. Res. Sect. B – Beam Interact. Mater. Atoms* **268**, 898–901.
- Feller C., Schouller E., Thomas F., Rouiller J. and Herbillon A. J. (1992) N₂-BET specific surface areas of some low activity clay soils and their relationships with secondary constituents and organic matter contents. *Soil Sci.* **153**, 293–299.
- Felmy A. R., Qafoku O., Arey B. W., Kovarik L., Liu J., Perea D. and Ilton E. S. (2015) Enhancing magnesite formation at low temperature and high CO₂ pressure: the impact of seed crystals and minor components. *Chem. Geol.* **395**, 119–125.
- Ferrini V., De Vito C. and Mignardi S. (2009) Synthesis of nesquehonite by reaction of gaseous CO₂ with Mg chloride solution: its potential role in the sequestration of carbon dioxide. *J. Hazard. Mater.* **168**, 832–837.
- Garber R. A., Harris P. M. and Borer J. M. (1990) Occurrence and significance of magnesite in Upper Permian (Guadalupean) Tansill and Yates formations, Delaware Basin, New Mexico. *AAPG Bull. – Am. Assoc. Petrol. Geol.* **74**, 119–134.
- Gautier Q., Bénézeth P., Mavromatis V. and Schott J. (2014) Hydromagnesite solubility product and growth kinetics in aqueous solution from 25 to 75 °C. *Geochim. Cosmochim. Acta* **138**, 1–20.
- Giammar D. E., Bruant R. G. and Peters C. A. (2005) Forsterite dissolution and magnesite precipitation at conditions relevant for deep saline aquifer storage and sequestration of carbon dioxide. *Chem. Geol.* **217**, 257–276.
- Hänchen M., Prigobbe V., Baciocchi R. and Mazzotti M. (2008) Precipitation in the Mg-carbonate system – effects of temperature and CO₂ pressure. *Chem. Eng. Sci.* **63**, 1012–1028.
- Hansen L. D., Dipple G. M., Gordon T. M. and Kellett D. A. (2005) Carbonated serpentinite (listwanite) at Atlin, British Columbia: a geological analogue to carbon dioxide sequestration. *Can. Mineral.* **43**, 225–239.
- Harrison A. L., Dipple G. M., Power I. M. and Mayer K. U. (2015) Influence of surface passivation and water content on mineral reactions in unsaturated porous media: implications for brucite carbonation and CO₂ sequestration. *Geochim. Cosmochim. Acta* **148**, 477–495.
- Harrison A. L., Dipple G. M., Power I. M. and Mayer K. U. (2016) The impact of evolving mineral-water-gas interfacial areas on mineral-fluid reaction rates in unsaturated porous media. *Chem. Geol.* **421**, 65–80.
- Harrison A. L., Mavromatis V., Oelkers E. H. and Bénézeth P. (2019) Solubility of the hydrated Mg-carbonates nesquehonite and dypingite from 5 to 35 degrees °C: implications for CO₂ storage and the relative stability of Mg-carbonates. *Chem. Geol.* **504**, 123–135.
- Harrison A. L., Power I. M. and Dipple G. M. (2013) Accelerated carbonation of brucite in mine tailings for carbon sequestration. *Environ. Sci. Technol.* **47**, 126–134.
- Hendy C. H. (1971) The isotopic geochemistry of speleothems – I. The calculation of the effects of different modes of formation on the isotopic composition of speleothems and their applicability as palaeoclimatic indicators. *Geochim. Cosmochim. Acta* **35**, 801–824.
- Hopkinson L., Kristova P., Rutt K. and Cressey G. (2012) Phase transitions in the system MgO-CO₂-H₂O during CO₂ degassing of Mg-bearing solutions. *Geochim. Cosmochim. Acta* **76**, 1–13.
- Hopkinson L., Rutt K. and Cressey G. (2008) The transformation of nesquehonite to hydromagnesite in the system CaO-MgO-H₂O-CO₂: an experimental spectroscopic study. *J. Geol.* **116**, 387–400.
- Kashchiev D. and van Rosmalen G. M. (2003) Review: nucleation in solutions revisited. *Cryst. Res. Technol.* **38**, 555–574.
- Każmierczak J., Kempe S., Kremer B., López-García P., Moreira D. and Tavera R. (2011) Hydrochemistry and microbialites of the alkaline crater lake Alchichica, Mexico. *Facies* **57**, 543–570.
- Königsberger E., Königsberger L. and Gamsjäger H. (1999) Low-temperature thermodynamic model for the system Na₂CO₃-MgCO₃-CaCO₃-H₂O. *Geochim. Cosmochim. Acta* **63**, 3105–3119.
- Lackner K. S., Wendt C. H., Butt D. P., Joyce, Jr., E. L. and Sharp D. H. (1995) Carbon dioxide disposal in carbonate minerals. *Energy* **20**, 1153–1170.
- Last F. M. and Last W. M. (2012) Lacustrine carbonates of the northern Great Plains of Canada. *Sediment. Geol.* **277**, 1–31.
- Léveillé R. J., Longstaffe F. J. and Fyfe W. S. (2007) An isotopic and geochemical study of carbonate-clay mineralization in basaltic caves: abiotic versus microbial processes. *Geobiology* **5**, 235–249.
- Lin Y. J., Zheng M. P. and Ye C. Y. (2017) Hydromagnesite precipitation in the Alkaline Lake Dujiali, central Qinghai-Tibetan Plateau: constraints on hydromagnesite precipitation from hydrochemistry and stable isotopes. *Appl. Geochem.* **78**, 139–148.
- Mees F., Castaneda C. and Van Ranst E. (2011) Sedimentary and diagenetic features in saline lake deposits of the Monegros region, northern Spain. *Catena* **85**, 245–252.
- Mees F. and Keppens E. (2013) Stable isotope geochemistry of magnesite from Holocene salt lake deposits, Taoudenni, Mali. *Geol. J.* **48**, 620–627.
- Melezhik V. A., Fallick A. E., Medvedev P. V. and Makarikhin V. V. (2001) Palaeoproterozoic magnesite: lithological and isotopic evidence for playa/sabkha environments. *Sedimentology* **48**, 379–397.
- Menounos B., Osborn G., Clague J. J. and Luckman B. H. (2009) Latest Pleistocene and Holocene glacier fluctuations in western Canada. *Quatern. Sci. Rev.* **28**, 2049–2074.
- Mihalynuk M. G., Smith M., Gabites J. E., Runkle D. and Lefebvre D. (1992) Age of emplacement and basement character of the Cache Creek Terrane as constrained by new isotopic and geochemical data. *Can. J. Earth Sci.* **29**, 2463–2477.

- Miller Q. R. S., Schaefer H. T., Kaszuba J. P., Qiu L., Bowden M. E. and McGrail B. P. (2018) Tunable manipulation of mineral carbonation kinetics in nanoscale water films via citrate additives. *Environ. Sci. Technol.* **52**, 7138–7148.
- Ming D. W. and Franklin W. T. (1985) Synthesis and characterization of lansfordite and nesquehonite. *Soil Sci. Soc. Am. J.* **49**, 1303–1308.
- Monger J. W. H. (1975) Upper Paleozoic rocks of the Atlin Terrane. Geological Survey of Canada, Paper 74-47, 63 p.
- Monger J. W. H. (1977a) Upper Paleozoic Rocks of Northwestern British Columbia, Current Research, Part A, Geological Survey of Canada, Paper 77-71 A, p. 255-262.
- Monger J. W. H. (1977b) Upper Paleozoic rocks of the Western Canadian Cordillera and their bearing on the Cordilleran evolution. *Can. J. Earth Sci.* **14**, 1832–1859.
- Monger J. W. H., Richards T. A. and Paterson L. (1978) The Hinterland Belt of the Canadian Cordillera: new data from northern and central British Columbia. *Can. J. Earth Sci.* **14**, 823–830.
- Montes-Hernandez G. and Renard F. (2016) Time-resolved in situ raman spectroscopy of the nucleation and growth of siderite, magnesite, and calcite and their precursors. *Cryst. Growth Des.* **16**, 7218–7230.
- Mook W. G., Bommerson J. C. and Staverman W. H. (1974) Carbon isotope fractionation between dissolved bicarbonate and gaseous carbon dioxide. *Earth Planet. Sci. Lett.* **22**, 169–176.
- Morse J. W. and Casey W. H. (1988) Ostwald processes and mineral paragenesis in sediments. *Am. J. Sci.* **288**, 537–560.
- O'Neil J. R. and Barnes I. (1971) C^{13} and O^{18} compositions in some fresh-water carbonates associated with ultramafic rocks and serpentinites: western United States. *Geochim. Cosmochim. Acta* **35**, 687–697.
- Oskierski H. C., Dlugogorski B. Z. and Jacobsen G. (2013) Sequestration of atmospheric CO_2 in a weathering-derived, serpentinite-hosted magnesite deposit: ^{14}C tracing of carbon sources and age constraints for a refined genetic model. *Geochim. Cosmochim. Acta* **122**, 226–246.
- Palmer D. A. and Wesolowski D. J. (1997) Potentiometric measurements of the first hydrolysis quotient of magnesium (II) to 250 °C and 5 molal ionic strength (NaCl). *J. Solut. Chem.* **26**, 217–232.
- Parkhurst D. L. and Appelo C. A. J. (2013) Description of Input and Examples for PHREEQC Version 3—A Computer Program for Speciation, Batch-Reaction, One-Dimensional Transport, and Inverse Geochemical Calculations, U.S. Geological Survey Techniques and Methods, Denver, Colorado, p. 497.
- Patterson C. S., Busey R. H. and Mesmer R. E. (1984) Second ionization of carbonic acid in NaCl media to 250°C. *J. Solut. Chem.* **13**, 647–661.
- Patterson C. S., Slocum G. H., Busey R. H. and Mesmer R. E. (1982) Carbonate equilibria in hydrothermal systems: first ionization of carbonic acid in NaCl media to 300°C. *Geochim. Cosmochim. Acta* **46**, 1653–1663.
- Pedrosa E. T., Boeck L., Putnis C. V. and Putnis A. (2017) The replacement of a carbonate rock by fluorite: kinetics and microstructure. *Am. Mineral.* **102**, 126–134.
- Pedrosa E. T., Putnis C. V. and Putnis A. (2016) The pseudomorphic replacement of marble by apatite: the role of fluid composition. *Chem. Geol.* **425**, 1–11.
- Poitevin E. (1924) A new occurrence of lansfordite from Atlin, BC. *Am. Mineral.* **9**, 225–228.
- Power I. M., Dipple G. M. and Francis P. S. (2017a) Assessing the carbon sequestration potential of magnesium oxychloride cement building materials. *Cem. Concr. Compos.* **78**, 97–107.
- Power I. M., Dipple G. M. and Southam G. (2010) Bioleaching of ultramafic tailings by *Acidithiobacillus* spp. for CO_2 Sequestration. *Environ. Sci. Technol.* **44**, 456–462.
- Power I. M., Harrison A. L. and Dipple G. M. (2016) Accelerating mineral carbonation using carbonic anhydrase. *Environ. Sci. Technol.* **50**, 2610–2618.
- Power I. M., Harrison A. L., Dipple G. M. and Southam G. (2013a) Carbon sequestration via carbonic anhydrase facilitated magnesium carbonate precipitation. *Int. J. Greenh. Gas Control* **16**, 145–155.
- Power I. M., Harrison A. L., Dipple G. M., Wilson S. A., Kelemen P. B., Hitch M. and Southam G. (2013b) Carbon mineralization: From natural analogues to engineered systems. In *Geochemistry of Geologic CO_2 Sequestration* (eds. D. J. DePaolo, D. R. Cole, A. Navrotsky and I. C. Bourg). The Mineralogical Society of America, Chantilly, Virginia, U.S.A., pp. 305–360.
- Power I. M., Kenward P. A., Dipple G. M. and Raudsepp M. (2017b) Room temperature magnesite precipitation. *Cryst. Growth Des.* **17**, 5652–5659.
- Power I. M., Wilson S. A., Harrison A. L., Dipple G. M., McCutcheon J., Southam G. and Kenward P. A. (2014) A depositional model for hydromagnesite–magnesite playas near Atlin, British Columbia, Canada. *Sedimentology* **61**, 1701–1733.
- Power I. M., Wilson S. A., Small D. P., Dipple G. M., Wan W. K. and Southam G. (2011) Microbially mediated mineral carbonation: roles of phototrophy and heterotrophy. *Environ. Sci. Technol.* **45**, 9061–9068.
- Power I. M., Wilson S. A., Thom J. M., Dipple G. M., Gabites J. E. and Southam G. (2009) The hydromagnesite playas of Atlin, British Columbia, Canada: a biogeochemical model for CO_2 sequestration. *Chem. Geol.* **260**, 286–300.
- Power I. M., Wilson S. A., Thom J. M., Dipple G. M. and Southam G. (2007) Biologically induced mineralization of dypingite by cyanobacteria from an alkaline wetland near Atlin, British Columbia, Canada. *Geochem. Trans.* **8**, 13.
- Pronost J., Beaudoin G., Tremblay J., Larachi F., Duchesne J., Hebert R. and Constantin M. (2011) Carbon sequestration kinetic and storage capacity of ultramafic mining waste. *Environ. Sci. Technol.* **45**, 9413–9420.
- Raade G. (1970) Dypingite, a new hydrous basic carbonate of magnesium, from Norway. *Am. Mineral.* **55**, 1457–1465.
- Renaut R. W. (1993) Morphology, distribution, and preservation potential of microbial mats in the hydromagnesite–magnesite playas of the Cariboo Plateau, British Columbia, Canada. *Hydrobiologia* **267**, 75–98.
- Renaut R. W. and Long P. R. (1989) Sedimentology of the saline lakes of the Cariboo Plateau, Interior British Columbia, Canada. *Sediment. Geol.* **64**, 239–264.
- Romanek C. S., Grossman E. L. and Morse J. W. (1992) Carbon isotopic fractionation in synthetic aragonite and calcite – effects of temperature and precipitation rate. *Geochim. Cosmochim. Acta* **56**, 419–430.
- Ruiz-Agudo E., Putnis C. V. and Putnis A. (2014) Coupled dissolution and precipitation at mineral–fluid interfaces. *Chem. Geol.* **383**, 132–146.
- Sade Z. and Halevy I. (2017) New constraints on kinetic isotope effects during $CO_{2(aq)}$ hydration and hydroxylation: revisiting theoretical and experimental data. *Geochim. Cosmochim. Acta* **214**, 246–265.
- Saldi G. D., Jordan G., Schott J. and Oelkers E. H. (2009) Magnesite growth rates as a function of temperature and saturation state. *Geochim. Cosmochim. Acta* **73**, 5646–5657.
- Saldi G. D., Schott J., Pokrovsky O. S., Gautier Q. and Oelkers E. H. (2012) An experimental study of magnesite precipitation rates at neutral to alkaline conditions and 100–200 degrees C as

- a function of pH, aqueous solution composition and chemical affinity. *Geochim. Cosmochim. Acta* **83**, 93–109.
- Santos G. M., Southon J. R., Druffel-Rodriguez K. C., Griffin S. and Mazon M. (2004) Magnesium perchlorate as an alternative water trap in AMS graphite sample preparation: a report on sample preparation at KCCAMS at the University of California, Irvine. *Radiocarbon* **46**, 165–173.
- Sanz-Montero M. E. and Rodríguez-Aranda J. P. (2012) Magnesite formation by microbial activity: evidence from a Miocene hypersaline lake. *Sediment. Geol.* **263**, 6–15.
- Schott J., Oelkers E. H., Bénézech P., Goddés Y. and François L. (2012) Can accurate kinetic laws be created to describe chemical weathering? *Comptes Rendus Geosci.* **344**, 568–585.
- Shock E. L. and Helgeson H. C. (1988) Calculation of the thermodynamic and transport properties of aqueous species at high pressures and temperatures: correlation algorithms for ionic species and equation of state predictions to 5 kb and 1000°C. *Geochim. Cosmochim. Acta* **52**, 2009–2036.
- Spotl C. and Burns S. J. (1994) Magnesite diagenesis in redbeds: a case study from the Permian of the Northern Calcareous Alps (Tyrol, Austria). *Sedimentology* **41**, 543–565.
- Stefánsson A., Bénézech P. and Schott J. (2014) Potentiometric and spectrophotometric study of the stability of magnesium carbonate and bicarbonate ion pairs to 150°C and aqueous inorganic carbon speciation and magnesite solubility. *Geochim. Cosmochim. Acta* **138**, 21–31.
- Swanson E. J., Fricker K. J., Sun M. and Park A. H. A. (2014) Directed precipitation of hydrated and anhydrous magnesium carbonates for carbon storage. *Phys. Chem. Chem. Phys.* **16**, 23440–23450.
- Thom J. M., Dipple G. M., Power I. M. and Harrison A. L. (2013) Chrysotile dissolution rates: implications for carbon sequestration. *Appl. Geochem.* **35**, 244–254.
- Wagman D. D., Evans W. H., Parker V. B., Schumm R. H., Halow I., Bailey S. M., Churney K. L. and Nuttall R. L. (1982) The NBS tables of chemical thermodynamic properties – selected values from inorganic and C₁ and C₂ organic substances in SI units. *J. Phys. Chem. Ref. Data* **11**, 1.
- Wilson S. A., Barker S. L. L., Dipple G. M. and Atudorei V. (2010) Isotopic disequilibrium during uptake of atmospheric CO₂ into mine process waters: implications for CO₂ sequestration. *Environ. Sci. Technol.* **44**, 9522–9529.
- Wilson S. A., Dipple G. M., Power I. M., Thom J. M., Anderson R. G., Raudsepp M., Gabites J. E. and Southam G. (2009a) Carbon dioxide fixation within mine wastes of ultramafic-hosted ore deposits: examples from the Clinton Creek and Cassiar chrysotile deposits, Canada. *Econ. Geol.* **104**, 95–112.
- Wilson S. A., Harrison A. L., Dipple G. M., Power I. M., Barker S. L. L., Mayer K. U., Fallon S. J., Raudsepp M. and Southam G. (2014) Offsetting of CO₂ emissions by air capture in mine tailings at the Mount Keith Nickel Mine, Western Australia: rates, controls and prospects for carbon neutral mining. *Int. J. Greenh. Gas Control* **25**, 121–140.
- Wilson S. A., Raudsepp M. and Dipple G. M. (2006) Verifying and quantifying carbon fixation in minerals from serpentine-rich mine tailings using the Rietveld method with X-ray powder diffraction data. *Am. Mineral.* **91**, 1331–1341.
- Wilson S. A., Raudsepp M. and Dipple G. M. (2009b) Quantifying carbon fixation in trace minerals from processed kimberlite: a comparative study of quantitative methods using X-ray powder diffraction data with applications to the Diavik Diamond Mine, Northwest Territories, Canada. *Appl. Geochem.* **24**, 2312–2331.
- Wright D. T. and Wacey D. (2005) Precipitation of dolomite using sulphate-reducing bacteria from the Coorong Region, South Australia: significance and implications. *Sedimentology* **52**, 987–1008.
- Young G. A. (1916) Hydromagnesite deposits of Atlin, B.C. Geological Survey of Canada Summary Report, 50-61.
- Zarandi A. E., Larachi F., Beaudoin G., Plante B. and Sciortino M. (2017) Nesquehonite as a carbon sink in ambient mineral carbonation of ultramafic mining wastes. *Chem. Eng. J.* **314**, 160–168.
- Zedef V., Russell M. J. and Fallick A. E. (2000) Genesis of vein stockwork and sedimentary magnesite and hydromagnesite deposits in the ultramafic terrans of southwestern Turkey: a stable isotope study. *Econ. Geol.* **95**, 429–446.
- Zhang P., Anderson H. L. J., Kelly J. W., Krumhansl J. L. and Papenguth H. W. (2000) Kinetics and mechanisms of formation of magnesite from hydromagnesite in brine, Sandia National Laboratories, Albuquerque.
- Zhao L., Sang L. Q., Chen J., Ji J. F. and Teng H. H. (2010) Aqueous carbonation of natural brucite: relevance to CO₂ sequestration. *Environ. Sci. Technol.* **44**, 406–411.

Associate editor: Dominik Weiss